# X-ray beam induced current analysis of CVD diamond detectors in the perspective of a beam tagging hodoscope development for hadrontherapy on-line monitoring

M.-L. Gallin-Martel, S. Curtoni, S. Marcatili, L. Abbassi, A. Bes, G. Bosson, J. Collot, T. Crozes, D. Dauvergne, W. de Nolf, et al.

# X-ray Beam Induced Current analysis of CVD diamond detectors in the perspective of a beam tagging hodoscope development for hadrontherapy on-line monitoring.

M.-L. Gallin-Martel[1a], S. Curtoni[a], S. Marcatili[a], L. Abbassi[b], A. Bes[a], G. Bosson[a], J. Collot[a], T. Crozes[b], D. Dauvergne[a], W. De Nolf[c], M. Fontana[d], L. Gallin-Martel[a], A. Ghimouz[a], J.-Y. Hostachy[a], A. Lacoste[a], J. Morse[c], J.-F. Motte[b], J.-F. Muraz[a], F. Rarbi[a], O. Rossetto[a], M. Salomé[c], E. Testa[d], M. Yamouni[a]

[a] Université Grenoble Alpes, CNRS, Grenoble INP, LPSC-IN2P3 UMR 5821, 38000 Grenoble, France

[b] Université Grenoble-Alpes, CNRS, Institut Néel, NANOFAB UPR2940, 38000 Grenoble, France

[c] ESRF, 38000 Grenoble, France

[d] Université de Lyon, CNRS, IP2I-IN2P3 UMR 5822, 69000 Lyon, France

**Keywords** CVD diamond, X-rays detection, Hadrontherapy monitoring

## Highlights

- Diamond double stripped beam monitor prototypes for hadrontherapy monitoring.
- Chemical Vapor Deposited diamond detector performance evaluated under X-rays.
- 2D current maps evaluated on diamond metallized surface using X-rays micro beams.
- Time resolution and bunch detection efficiency at contact strip crossing points.

## Abstract

The intrinsic electronic properties of diamond make it suitable for radiation-hard and very fast detector development with good signal to noise ratios. With the advent of new generations of ion accelerators either for physics (nuclear and high energy physics) or medical applications (hadrontherapy and synchrotron radiation radiotherapy) there is a need for a very accurate beam monitoring in high radiation environments. Diamond is particularly suited to these applications. Fast pulse detection mode for time stamp, and current integration mode for operation as beam monitors at high particle rates are targeted. Commercial single-crystal, polycrystalline and heteroepitaxial diamonds produced by Chemical Vapor Deposited (CVD) method are analyzed and compared by means of X-ray Beam Induced Current (XBIC). Their performance as particle detectors is investigated using a 8.5 keV X-ray photon micro-bunch beam at ESRF (European Synchrotron Radiation Facility). This facility provides a focused (~1 μm) pulsed beam (100 ps bunch duration), producing an almost uniform energy deposit along the beam irradiated volume in the detector, therefore closely mimicking the interaction of single charged particles. The XBIC set-up of the ID21 beamline enabled us to draw 2D response maps of detectors with disk- and strip metal contact patterns. Using the pulse-synchronized XBIC measurements, a time resolution of 150 ps RMS and bunch detection efficiency of ~100 % were evaluated at the contact strip crossing points of a first prototype polycrystalline beam monitor.

[1] Corresponding author. Tel.: +33 4 76 28 41 28; fax: +33 4 76 28 40 04. LPSC, 53 Avenue des Martyrs 38000 Grenoble-FRANCE

E-mail address: mlgallin@lpsc.in2p3.fr

## 1. Introduction

Compared to other semiconductor detectors, diamond-based detectors exhibit several advantages. A high resistivity (>$10^{13}$ Ω m) due to its wide electronic band gap (5.48 eV) results in an almost negligible leakage current and the low dielectric constant (~5.72) in practice results in lower preamplifier noise levels as compared to silicon devices of similar geometry. The high diamond mobility for both charge carriers [1] also results in a very fast detector response, enabling tens of picoseconds time resolution and high count-rate capabilities [2]. Diamond detector applications are therefore more and more considered in various fields, such as high-energy and nuclear physics [3], and medical applications [4], [5], [6], [7], [8].

The development of new generations of ion accelerators either for physics (nuclear and high-energy physics) or medical applications (hadrontherapy and synchrotron radiation radiotherapy) generates the need for a very accurate beam monitoring with precise and fast counting in these high radiation environments. Diamond is well suited to these areas of application [8], [9], [10], [11], [12], [13].

The development of a diamond-based beam monitor is part of a large-scale French experimental project emanating from the national collaboration CLaRyS and intended for online monitoring of hadrontherapy [14]. Hadrontherapy is an alternative cancer therapy that consists in the treatment of tumors by light ion beams (e.g. carbon or protons). The ions deposit a large fraction of their dose at the end of their path, in the so-called Bragg peak. As compared with conventional photon radiotherapy, this allows a more efficient dose delivery in the tumor, with a reduction of the dose deposited in the nearby healthy organs. The conformation of the deposited dose to the tumor volume is provided by distributing spread-out Bragg peaks in the target volume, either spot by spot, or by means of passive scattering and energy degradation. However, since multiple sources of uncertainty in the ion range may cause deviations from the planned dose distribution [15], online control of the ion range is desired in order to improve safety margins and optimize the ballistic advantage of ion therapy.

During an irradiation with ion beams, nuclear reactions occur for a fraction of the incident projectiles. Photons in the range 1-10 MeV are emitted almost isotropically within a picosecond after such reactions. It has been shown experimentally that the longitudinal distribution of such prompt-gamma production is highly correlated to the primary ion range [16], [17], [18].

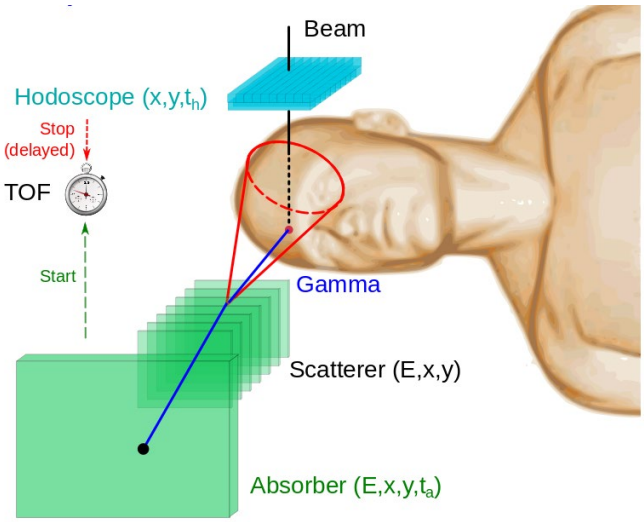


Figure 1 Scheme of the combination of a Compton camera and a beam hodoscope for Time of Flight prompt-gamma range verification.

Based on these observations, two systems for prompt gamma detection are currently under development in the CLaRyS collaboration [19], [14]: a collimated gamma camera, and a Compton camera (Figure 1). The originality of the two systems is the use of Time of Flight (ToF) in order to reject the background induced by secondary particles. Depending on the beam time-structure and intensity, a beam tagging hodoscope may be necessary to detect the arrival times of ion bunches or even individual projectiles. This hodoscope will be also used for transverse position measurement, giving access to 3D prompt-gamma imaging. Thus the hodoscope plays a major role in all the detection concepts, and has to fulfil the requirement of providing both position and timing information of the incident hadron beam at about 100 Mcps count rates. As an alternative to a large-area scintillating-fiber hodoscope already under construction [14], a diamond-based hodoscope is being developed which presents the advantages of fast response and high radiation tolerance. The device must operate in hadrontherapy, in a harsh radiation environment with a long operational lifetime, withstanding radiation damage. The strong covalent bonds, large band gap and small neutron cross section all contribute to making diamond a radiation hard material [4], [20], [21]. The radiation hardness of diamond compared to that of the widespread silicon technology can be demonstrated by the SRIM simulation software. It was already shown that the number of vacancies generated by an incident carbon ion beam of 400 MeV/u (a typical carbon beam energy used in hadrontherapy) is only 1300 per incident ion in diamond, compared to 3500 in silicon [22]. Reference [23] describes the behaviour of sCVD and pCVD diamond detectors as irradiated by 70 MeV and 800 MeV protons for fluences up to ~$10^{16}$ p/cm$^2$ . A significant decrease of the charge-trapping mean free path was observed in sCVD diamonds at such fluences, with a less pronounced effect observed for pCVDs. However, such fluences correspond to several years of operation in clinical conditions.

This diamond beam monitor will be equipped with the largest available sensors. The detectors will be segmented with double side orthogonal metallic strips readout (X and Y directions), in order to provide spatial resolution while maintaining low detector capacitance values. Diamonds will be assembled in a mosaic arrangement to cover the needed detection area (typically 1 cm$^2$ or 4 cm$^2$). Finally, a further specific goal of the whole project is the development of dedicated readout electronics (fast preamplifier, current integration) using designs based on both discrete and integrated components (CMOS 130 nm ASICS), and a data acquisition system [24] which is compliant with the CLaRyS µTCA acquisition system [25]. The current integration front-end electronics must satisfy the requirements of the beam time structure and ensure a linear response to the beam intensity variation over a wide dynamic range. Using a 500 µm thick single crystal Chemical Vapor Deposited (sCVD) diamond detector, this represents a charge ranging typically from 7.5 fC for protons of 70 MeV , up to 520 fC for carbon ions of 95 MeV/nucleon, in a pulse of some nanoseconds, regards to the high mobility of charge carriers in diamond.

Commercial CVD single-crystal, poly-crystalline and heteroepitaxial diamonds were acquired. These were processed and characterized with short-bunched 8.5 keV photons from the European Synchrotron Radiation Facility (ESRF). Third generation Synchrotron facilities offer the capability of highly focused beams, to <1 µm FWHM. As regards energy deposition in the diamond, in the ESRF 4-bunch machine mode, the X-ray pulses are of ≈100 ps duration spaced at 704 ns intervals, and thus mimic the passage of single ionizing particles. Indeed, their exponential absorption length 1/µ~750 µm [26] results in an energy deposit which is almost uniformly distributed over the whole thickness of our samples (300 - 500 µm). We characterized the temporal and charge/current signal responses of several diamond detectors over a large fraction of their surfaces. The possible application of diamonds as a position sensitive detector is discussed in the present paper from these radiation test results. The respective performances in terms of surface detection homogeneity of large area (~1 cm$^2$) polycrystalline- and heteroepitaxially-grown diamonds are compared to single-crystal diamond detectors. Finally, an X-ray analysis of a double side striped polycrystalline diamond surface equipped as first beam monitor prototype was performed. Diamond detector performances were analyzed both in current integration

and in pulsed modes. The X-ray detection efficiencies and the time resolutions were evaluated at various top-bottom strip crossing points.

## 2. Material and methods

### 2.1 Diamond sensors

CVD synthetic diamonds are grown by the technique of microwave plasma-enhanced CVD [27]. Single crystal sCVD diamonds are almost free from defects acting as charge traps, but their available area is restricted 1cm$^2$ (1 cm$^2$ is still considered as an upper limit, not available on-shelf). Polycrystalline pCVD diamonds present grain boundaries and stacking faults, structural defects which act as undesirable charge trapping centers for free charge carriers. The main interest in pCVD material is that it can be grown as wafers to sizes > 6 inches [28]. Lastly, heteroepitaxially grown diamonds, hereafter referred to as Diamond On Iridium (DOI), were tested. Such diamonds are also grown as wafers, with areas > 1 cm$^2$ cut from a parent wafer after substrate removal [29], [30].

In the present study, we used both sCVD and pCVD diamonds from Element6 [28], and heteroepitaxially grown DOI diamonds from Audiatec and the University of Augsburg [29], [30]. The samples tested ranged from 300 µm to 500 µm in thickness, and with areas from 0.45 × 0.45 cm$^2$ to 1 × 1 cm$^2$. The suitability of these diamonds as detectors was first investigated by measuring their current voltage characteristics, as illustrated by Figure 2. Similar measurements were made previously [31] [32], carried out at room temperature and ambient pressure. The detectors were in darkness with electromagnetic shielding, with a bias voltage applied to one side of the detector. The current generated by the detector, without external excitation other than the electric field created by the bias voltage, was measured from the opposite, ground potential side using a Keithley 6487 picoammeter, of minimum resolution of ± 10 fA (for a range of 2 nA). All the diamonds thus tested had aluminum contacts except (and only for these preliminary tests) the sample DOI-1 (which was not metallized) and a 300 µm thick pCVD sample (which was contacted with silver lacquer). Except for DOI-1, all the diamonds showed an asymmetry in their leakage current measurements for positive and negative applied bias voltage. This asymmetric behavior revealed non Ohmic contacts that showed rather Schottky-like behaviour. The observed assymetry probably resulted from the choice of the aluminum layer deposited on the diamond top and bottom sides as in [33] and variations in the diamond surface preparation made before the contact metallization. Note also that the values of the leakage currents were several orders of magnitude higher on the DOI samples (except for DOI-2) compared to those of pCVD. This observation may indicate, *a priori*, evidence of difference in crystal quality between the various detectors and that is discussed later in this paper. Aluminum contacts have already proven their efficiency for detectors of traversing ionizing particles and for X-rays [33] [34]. Contacts such as TiPtAu are known to exhibit a more ohmic behaviour [35], but they were not used in our tests in order to minimize soft X-ray absorption in the contacts themselves [36].

These leakage current measurements enabled us to characterize the response of the diamond detectors in pulse mode and define an optimal bias for the XBIC experiments. To estimate their charge collection efficiencies, the diamond detectors were also characterized with a $^{241}$Am 5.5 MeV alpha particle test bench. A detailed study, reported in [37], concludes that the 0.45 × 0.45 cm$^2$ × 500 µm sCVD sample exhibited an overall charge collection efficiency of ≈100 % as compared to ≈30 % for the 1 × 1 cm$^2$ × 300 µm pCVD sample, and ≈40 % for the 0.5 × 0.5 cm$^2$ × 300 µm DOI sample from the University of Augsburg. This last observation is indicative of the density of defects in the crystal structure of the diamonds tested and also reveals the overall behavior of the detectors under exposure to weakly penetrating ionizing particle radiation.

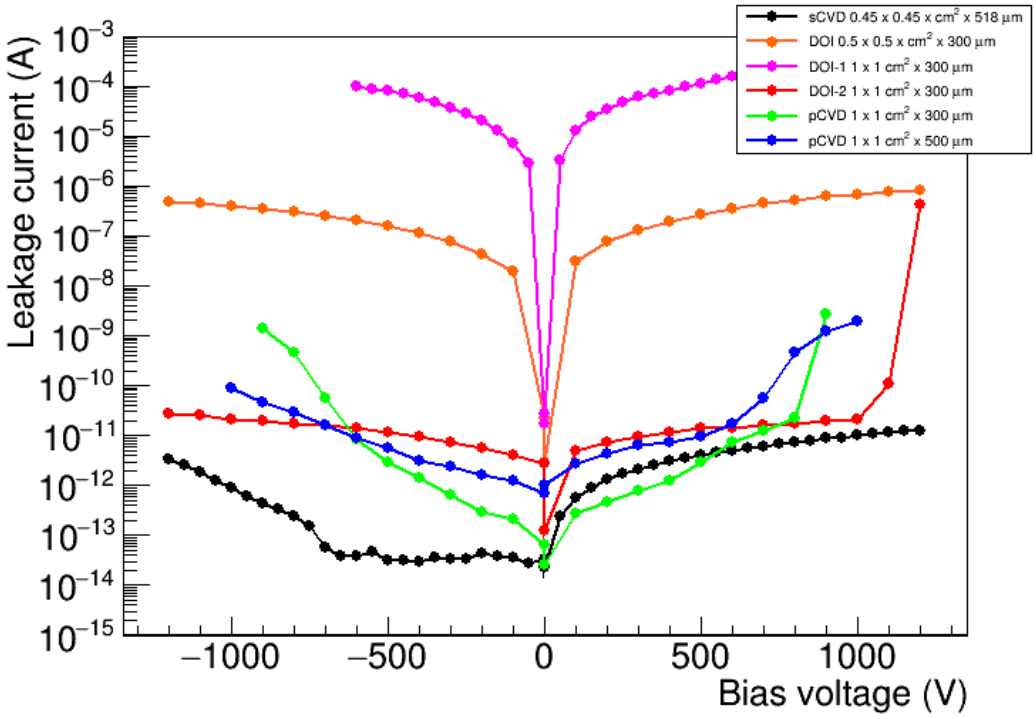


Figure 2: Leakage currents versus the bias voltage. All the diamond samples exhibit aluminum contacts except DOI-1 (not metallized) and the 300 µm thick pCVD (metallized with silver lacquer).

## 2.2 Detector processing

The aluminum disk shaped metallization was locally performed using Distributed Microwave Plasmas (DMW) deposition, a technology developed at LPSC [38]. The sensor contact, as detailed in references [31], [32] for the disk-shaped metallization consists of a 50 nm thick aluminum layer deposited on both sides. The diamond is sandwiched between two printed circuit boards (PCB). A plastic spacer is used to avoid damage to the diamond while the two PCBs are screwed together. The electrical contact is ensured by a copper ring which surrounds a window opening in the PCB that reveals the contacted diamond. The diamond holders provide direct connection to 50 Ω impedance SMA connectors. These enable reversible bias and signal readout connections to either side of the diamond. At ESRF, the detector holder was also enclosed in an electromagnetic-shielding box (Figure 3 (a)) with kapton tape covered apertures for the X-ray beam passage.

Three hodoscope prototypes were built. One was equipped with a pCVD diamond and two with DOI diamonds (all were 1 × 1 cm² × 300 µm in size). Each diamond was equipped with a unique, double-side strip metallized diamond sensor [32]. The strips on opposing sides are arranged orthogonally, enabling X and Y spatial localization. The lift-off process was used to produce the strips. It consists in creating structures (patterning) using a sacrificial material (e.g., photoresist). This was performed at the NANOFAB laboratory as described in reference [32]. The resulting metallization on the diamond sensor consists of 8 strips of 950 µm width separated by a 100 µm gap, surrounded by a guard ring (see Figure 5 (a) and Figure 5 (b) for the detailed schematic). Only one DOI diamond exhibited a non-regular size gap (Figure 5 (b)). The choice of the guard ring is based on the desire to reduce edge effects, which is essential for this type of detector intended for spatial localization.

Unlike the case of the disk-shaped metallization, wire bonds ensured the electrical connection between each diamond strip and the PCB. This led us to make a thicker deposit of aluminum for the strip electrodes to avoid contact tearing when placing the bonding wires. In addition, a set of discrete current amplifiers designed at LPSC (1 GHz bandwidth with 30 dB gain) were mounted on the circuit board. The entire assembly was placed inside an electromagnetic shielding box provided with SMA connectors to enable biasing and analog signal readout for each strip (Figure 3 (b)).

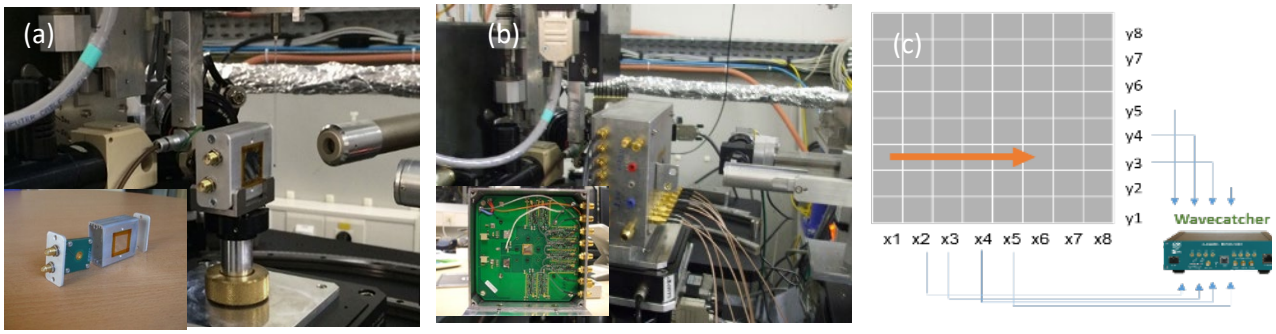


Figure 3: (a) Detector holder for disk metallized diamond and (b) the 1 $cm^2$ double side striped pCVD diamond mounted on the PCB inside respectively in their electromagnetic shielding box and under test on the ID21 beam line at ESRF. (c) details for 1$cm^2$ pCVD detector beam scanning scheme of the tracks with signal readout using the Wavecatcher acquisition system.

### 2.3 XBIC experimental set-up

The diamond detectors operate as solid state ionization chambers. The bias voltage (typically 1V/µm) is applied on one side of the diamond and the signal readout is performed on the opposite side which is at ground potential. The shielding box containing the diamond holder that corresponds to either the disk or striped metallized samples was attached to a magnetic kinematic mount, which provided micron positioning reproducibility at the sample position of the micro-diffraction end station (in air) of the ID21 beamline at ESRF (Figure 3 (a) and (b)).

The diamond detectors were placed in between two Si p-i-n diodes used for beam intensity normalization purposes as illustrated on the schematic drawn in Figure 4. The diode located upstream of the diamonds relative to the beam is denoted as Iodet. Iodet is a diode with a central hole to enable beam passage. This diode is excited by X-rays scattered by a thin Ti layer deposited on a $Si_3N_4$ foil placed just upstream. The diode collects the fluorescence of Ti and gives a signal proportional to the incident intensity. The diode located downstream is denoted as Idet. Two different data running modes were used during the whole experiment: current integration mode (diamond signal currents measured with electrometers) and the signal pulse readout mode (diamond signal into 50 Ω input impedance fast amplifiers).

To draw current maps in current integration mode, three Keithley 485 picoammeters were used (named Pico 3 and Pico 1 for those connected respectively to Iodet and Idet, and K485 for those connected to the diamond samples). Each Keithley analog voltage output was coupled to a voltage-to-frequency converter read out by a standard ESRF counter board. This system was configured to provide 100 ms current integration periods that could be synchronized to position scans of the diamonds in the X-ray beam. For the signal pulse readout mode, the disk metallized diamond signal output was connected to a CIVIDEC C2 low-noise broadband amplifier (2 GHz, 40 dB from CIVIDEC Instrumentation Company [39]). This exhibits a 50 Ω input impedance and is designed to work with FWHM pulse widths of less than 1 ns. The signal measurements were measured alternatively with a 500 MHz, 3.2 GS/s digital sampling 'WaveCatcher' [40] system, and with a 2 GHz, analog bandwidth 20 GS/s Digital Sampling Oscilloscope (DSO LeCroy 620Zi) [41]. These systems could be configured for readout by the ID21

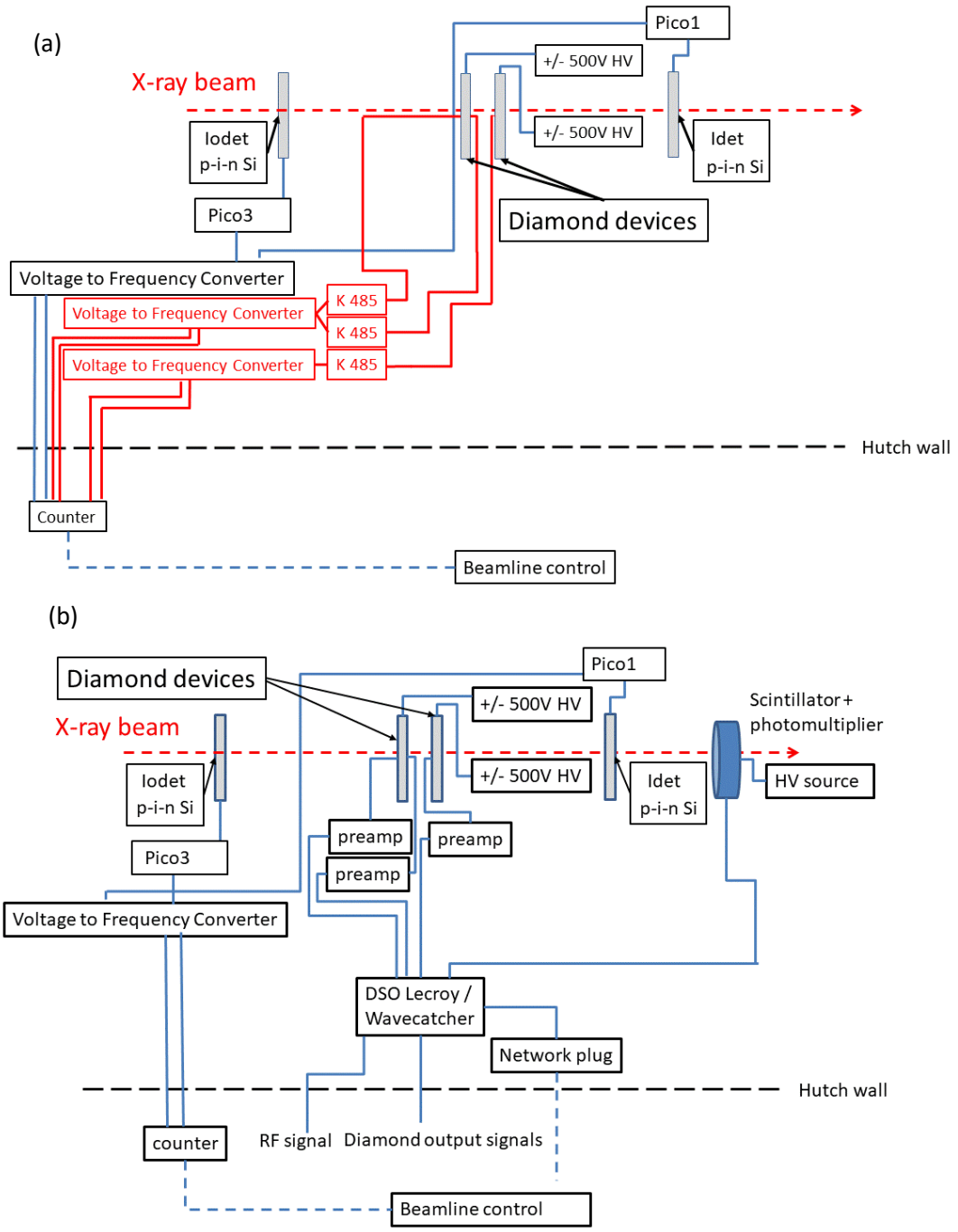


Figure 4 Schematic of the diamond devices set-up at ESRF on ID21 beam line in current mode (a) and in pulse mode (b). Iodet is a diode with a central hole to enable beam passage.

beamline data acquisition system in a continuous acquisition mode, recording a set of waveforms, thus enabling large data statistics for offline analysis. In signal pulse readout mode, the timing of the data acquisition for each pulse readout was precise at a level <1 ns with respect to the incidence of the X-ray beam pulses on the diamonds: this was achieved by trigger-locking the acquisition systems to a reference signal that was a sub-multiple of the ESRF synchrotron 352 MHz radiofrequency. The DSO and Keithley 485 acquisitions were both fully integrated into the ID21 SPEC software acquisition framework

which enabled us to measure the response of the detectors as they were motor-scanned across the beam. Furthermore, the 8 channels readout available on the WaveCatcher made it possible to record 4 strips in X and 4 strips in Y while the first diamond-based beam monitor prototype was motor scanned across the beam (Figure 3 (c)); and thus evaluate its beam detection efficiency and time resolution performance at the precision level of the X-rays ID21 micron-sized beam, focusing on specific diamond areas of interest which could be selected by the analysis of previous area- or line- scans made with the Keithley current mode set-up.

### 2.4 Summary of the diamond samples tested at ESRF versus data acquisition set-up and data analysis mode.

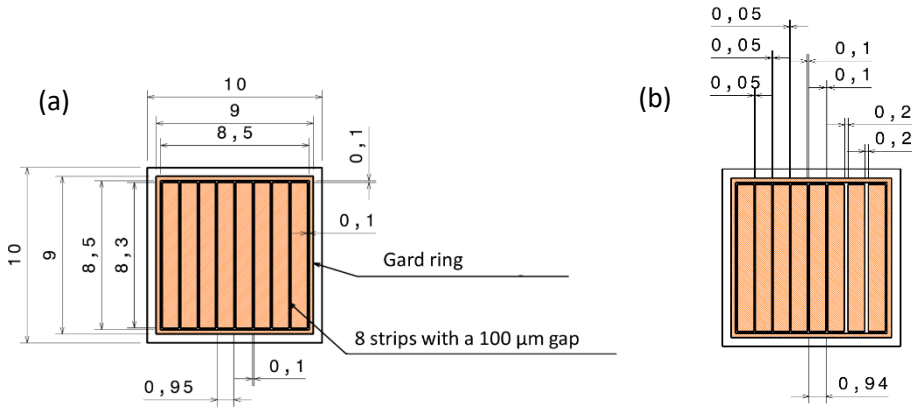


Figure 5 Details of the 8 strips distribution over the tripped diamond surface in the case of the regular spacing (a) and the non-regular one (b).

| Diamond Material | Manufacturer | Electrode | Read-out amplifier | Data acquisition | Acquisition mode |
|---|---|---|---|---|---|
| sCVD<br>$0.45 \times 0.45\ cm^2 \times 518\ \mu m$ | Element 6 | Disk | CIVIDEC C2 | Lecroy DSO | Pulse mode |
| pCVD<br>$1 \times 1\ cm^2 \times 500\ \mu m$ | Element 6 | Disk | none | Keithley | Current integration |
| pCVD<br>$1 \times 1\ cm^2 \times 300\ \mu m$ | Element6 | 8 strips with regular spacing | none | Keithley | Current integration |
| | | | LPSC | Wavecatcher | Pulse mode |
| DOI<br>$0.5 \times 0.5\ cm^2 \times 300\ \mu m$ | Augsburg University | Disk | none | Keithley | Current integration |
| DOI-1<br>$1 \times 1\ cm^2 \times 300\ \mu m$ | Audiatec | 8 strips with regular spacing | none | Keithley | Current integration |
| DOI-2<br>$1 \times 1\ cm^2 \times 300\ \mu m$ | Audiatec | 8 strips with non-regular spacing | none | Keithley | Current integration |

Table 1 Summary of the various diamond detector configurations used

A summary of the diamond samples tested during the XBIC experiment is presented in Table 1. In Figure 5 (a) the details of the regular 8 strips distribution on the surface for the pCVD and DOI-1 diamond $1 \times 1\ cm^2 \times 300\ \mu m$ samples are presented. On DOI-2 ($1 \times 1\ cm^2 \times 300\ \mu m$) Figure 5 (b) the strip intervals vary from 50 µm to 200 µm. DOI-2 has been metallized with strips spaced with a variable pitch to assess the load sharing capacities between two neighboring strips.

One of the first objectives of the X-ray beam test was to check the homogeneity of each diamond response over its whole surface and to compare detector performances versus diamond growth process. To do this, a calibration technique in current mode was developed to make a surface mapping comparison between the different diamond samples (sCVD, pCVD and DOI, see Table 1).

### 2.5 Surface mapping procedure in current integration mode

***a) X-ray flux calibration.***

Beam flux measurements were made at the very beginning of the experiment when no diamond sample was placed in between the two p-i-n diodes. With the 8.5 keV X-ray beam turned on, the beam flux Φ(ph) measured in number of photons per seconds (ph/s) can be calculated as follows:

$$\Phi(\mathrm{ph}) = (\mathrm{I_{pico1}} - \mathrm{I_{darkpico1}}) \times \frac{\mathrm{E_{eh\,/Si}} \times \mathrm{Times}}{\mathrm{E_{ph}} \times \mathrm{e} \times \mathrm{T_0}}, \quad (1)$$

where:

- $I_{pico1}$ is the current measured on the Keithley 485 picoammeter connected to the Idet p-i-n diode (A),
- $I_{darkpico1}$ is the value of $I_{pico1}$ measured when the beam is off (380 pA),
- $E_{eh/Si}$ is the energy to create electron-hole pairs in silicon (~3.6 eV),
- Times is the time measured in seconds during which a data acquisition was done at a given beam position on the sample surface
- $T_0$ is the reference time used for a normalization purpose ($T_0$=1 s),
- $E_{ph}$ is the X-ray energy (8.5 keV),
- e is the electron charge ($1.602\ 10^{-19}$ C).

In the 4 bunch operation mode of the ESRF synchrotron, the nominal value of the injected synchrotron ring current was 32 mA. However, typically during a given period of 20 minutes, this current decreased quasi-exponentially to reach ~20 mA before a beam refill was carried out over few minutes to again reach the initial value of 32 mA, and so on for the entire duration of a data acquisition run. When the ESRF synchrotron current was at its maximum 32 mA we measured $I_{pico1} = 6.7\ 10^{-7}$ A, and from (1), we calculated $\Phi_{32mA}(\mathrm{ph}) = 1.79\ 10^{9}$ ph/s. This represents 1340 photons in a single bunch.

***b) X-ray current calibration.***

For each diamond sample motor-scanned in the beam, three surface maps were recorded simultaneously: one for each p-i-n diode, and one for the diamond sample itself. The diode located upstream is not placed directly in the beam but detects scattered photons. One would expect from the recorded map a very homogeneous data distribution over the whole surface. All the points of each map were stored in n × p matrices, where n and p are respectively the row and column numbers in the 2D maps. The calibrated matrix for the diamond sample is measured in nA units, corrected (i.e. normalized) for the time decreasing beam intensity between the synchrotron storage ring refills as described in 2.5 a).

And, finally, a transmitted map $M_{transmitted}$ has been drawn using the formula:

$$M_{transmitted} = \frac{I_{ph-out}}{I_{ph-in}}. \qquad (2)$$

Where $I_{ph\_out}$ and $I_{ph\_in}$ are the matrix of current values measured on each p-i-n diode situated respectively dowstream and upstream the diamond sample.

## 2.6 Surface mapping procedure in the pulse readout mode

***a) Signal recording and mean current calculation***

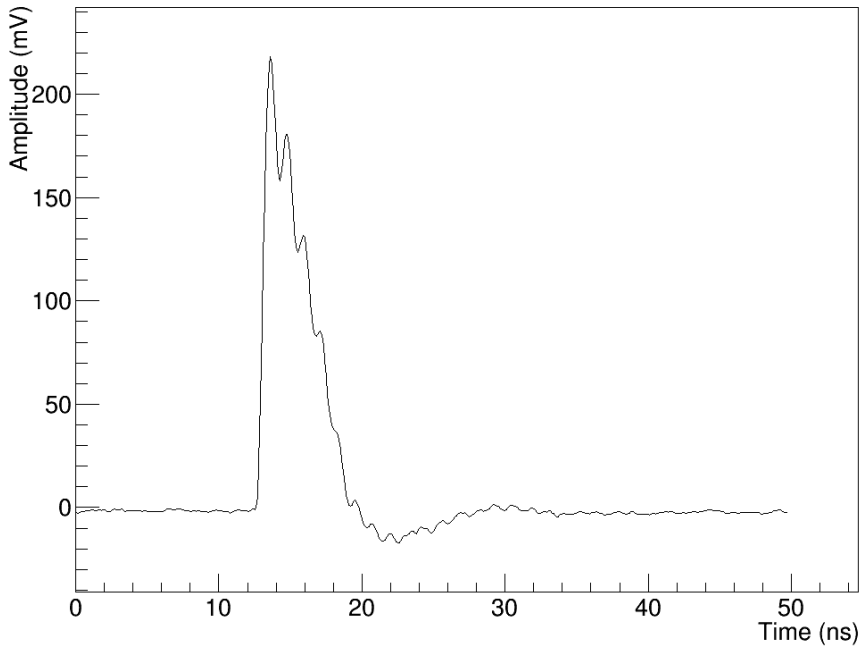


Figure 6 sCVD signal waveform recording using the DSO set-up (500 time points separated by 100 ps).

The diamond samples were also motor-scanned across the beam while their output signals were recorded using the Lecroy DSO set-up. This technique enabled us to perform simultaneously current mapping

(although less precise by comparison with the current mode described previously) and diamond response waveform analysis (the main objective of this type of mode). The acquisition window was optimized and fixed for the entire duration of data recording. Average waveform time trace (Figure 6 for sCVD output signal) was evaluated over 64 DSO triggers by the DSO itself, and this averaged trace consisting of 500 time points spaced by 100 ps read-out by the data acquisition system and stored for an offline analysis purpose at each point of the diamond surface. Taking as an example the case of the sCVD diamond with a surface of $0.45 \times 0.45$ cm$^2$, a total of 8281 points spaced 50 µm apart were recorded to create the surface map of the diamond sample. An offline procedure was used to calculate the average value of the current, $I_{mean}$ at each position point as follows: the baseline of each signal is calculated on the first 50 bins of each waveform time trace just prior to the arrival time of the X-ray pulse. The quantity Q of charges measured is deduced from calculation of the signal integrated over the entire recorded trace period with the baseline subtracted value. The average current intensity measured in nA units in each point of the map is then calculated as follows:

$$I_{mean} = \frac{Q}{T_{beam}} = \frac{\sum_i V_i \times t_{bin}}{R \times Gain \times T_{beam}}, \qquad (3)$$

where

- $V_i$ is the signal voltage value after baseline subtraction, measured at bin number i on the waveform distribution recorded with the Lecroy DSO set-up,
- $t_{bin}$ is the value in nanoseconds of the time scale on the Lecroy DSO set-up for the waveform data acquisition,
- R is the value of the input impedance (50 Ω),
- Gain is the nominal value of the preamplifier gain, in the present experiment CIVIDEC C2 ones are concerned, we use the nominal value of 40 dB given by that manufacturer, although we did not measure this for each preamplifier,
- $T_{beam}$ relies on the beam delivery time in the very specific 4 bunch mode at ESRF and is equal to 704 ns, which corresponds to the beam intervals between two consecutive beam pulses.

***b) ESRF beam current calibration***.

As explained above, in the 4 bunch operation mode of the ESRF, the initial value of the synchrotron storage ring current during the present experiment was 32 mA. During a given measurement period, the current value decreases before a beam refill is carried out (refills occurred at intervals ranging from 20 to 60 minutes), to reach again the initial current value of 32 mA, and so on for the entire duration of data acquisition. Unfortunately, it was not possible to record precisely the beam intensity variations in time necessary to normalize the recorded diamond output signals. Consequently, such maps are not normalized to the beam intensity.

## 3. Results and discussion of the performances of various diamond samples in current mode.

### 3.1 Single crystal diamond (sCVD).

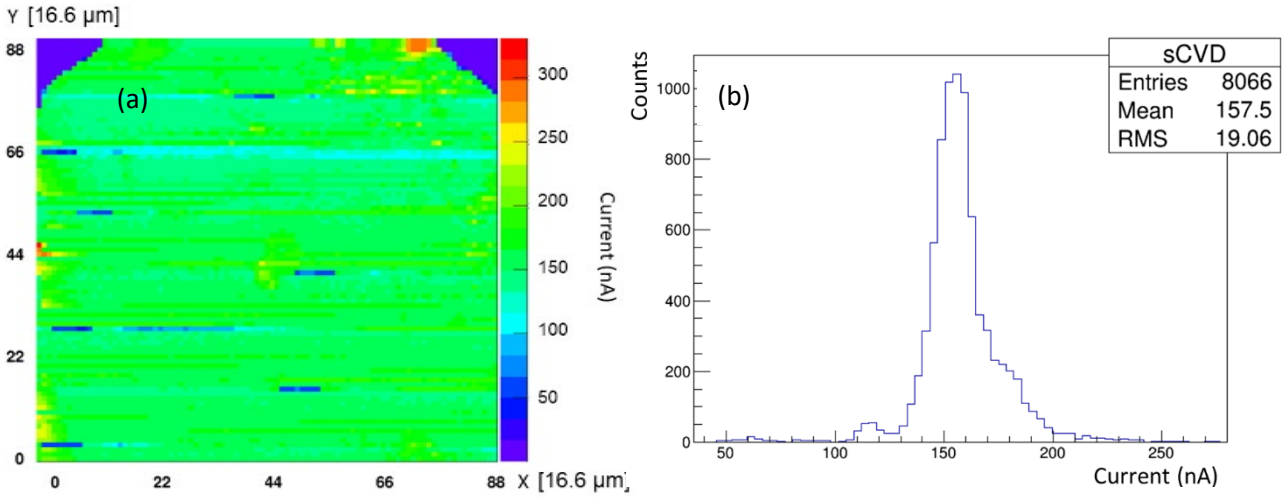


Figure 7 Histogram of the measured current (a) on the surface map (b) of a 0.45×0.45 $cm^2$×518 µm sCVD diamond detector from Element 6.

In Figure 7 a current map is shown for a 0.45 × 0.45 cm² × 518 µm sCVD diamond detector from Element 6. The current was not measured with the Keithley electrometer but signal pulse waveforms were recorded with the DSO from Lecroy and current values were deduced from off-line analysis (using pulse integration, see section 2.6). The diamond was biased at +500 V, the whole diamond surface was characterized with a scan position stepping size of 16.6 µm, and the signal integration time at each point was set to 1 s. Periodic horizontal lines can be observed that arise from the beam refill every 60 minutes in this particular bunch mode configuration. These beam variations affect the results. The dark blue segments are correlated with the beam refill. The sudden beam increase process leads to an injection of charges. At first it was observed that the diamond signal decreased strongly (dark blue segment) before going up (yellow segment). It should be mentioned here that the 2D map is filled from left to right at each row. Charge may certainly saturate traps inducing trap priming which leads then to an overshoot due to the space charge build up, as described in [42]. Anyway, the diamond response is very homogeneous if we exclude a singular point at the top right corner on Figure 7 (a) which is located near the circular collection electrode. This suggest a beam-induced charge injection from a defective surface site. Similar results were obtained [36] at ESRF with electronic grade sCVD samples which were patterned with Ni-TiC contacts: a uniform spatial response - flat within 0.2% - was seen when the devices were mapped with a sub-micron synchrotron collimated X-ray beam. Furthermore, X-ray beam absorption occurring in the Ti metal layers was also quantified. As previously discussed in section 2.1, this study, conducted by some of the authors of present paper, guided our choice towards the use of aluminum contact rather than titanium based ones."

Assuming that the integral of the current over each pulse must be equal to the total charge $Q_{beam}$created:

$$Q_{beam} = \frac{\Phi_{32mA(ph)} \times T_{beam} \times E_{ph} \times R_{diamond} \times e}{E_{eh/diamond}}, \quad (4)$$

where $\Phi_{32mA}$(ph) has been calculated before and was found equal to 1.79 $10^9$ ph/s, $E_{ph}$ and $T_{beam}$ have the same definitions as those used in equation (1). $E_{eh/diamond}$ is the required energy in diamond to create electron hole pairs (13.6 eV [43] [44]). Finally, $R_{diamond}$ is the fraction of the beam energy deposited in the diamond thickness, which can be calculated as follows:

$$R_{diamond} = 1 - \frac{I_{ph-out}}{I_{ph-in}} = \left(1 - e^{-\mu\rho d}\right), \qquad (5)$$

where:

- $\mu$ is the mass absorption coefficient (for 8.5keV photons in carbon , $\mu$=4.025 $cm^2g^{-1}$),
- $\rho$ is the mass density (3.517 g $cm^{-3}$),
- d is the diamond sample thickness (518 µm).

Using the known mass density of single crystal diamond of 3.517 g $cm^{-3}$, equation (5) leads to an energy deposition per individual X-ray beam pulse in the 518 µm thick sCVD diamond: $E_{diamond}$ = 5.2 MeV. This implies that $Q_{beam}$ = 61 fC and $I_{mean} = Q_{beam}/T_{beam}$ = 86 nA.
The difference between calculation and measurement can be explained by the fact that the gain of the CIVIDEC C2 used is not precisely known, while in equation (3) a nominal value of 40 dB was used to calibrate the map in Figure 7. The calculated value 86 nA would correspond to a real amplifier gain of 45 dB. This analysis also assumes complete charge collection within a sCVD diamond, which has been confirmed in previous laboratory measurements we performed with an $^{241}$Am 5.5 MeV alpha source test bench [37].

### 3.2 Polycrystalline diamond (pCVD)

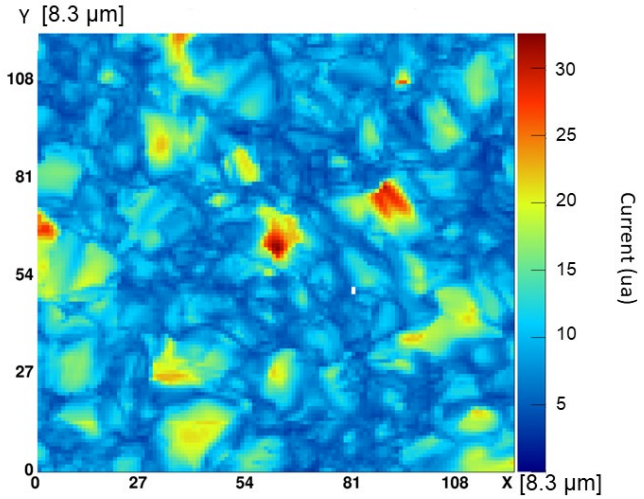


Figure 8 Surface map (1 $mm^2$) of a 1 × 1 $cm^2$ × 500 µm pCVD from Element 6.

Surface mapping of several detectors was first performed using the current integration mode. Figure 8 shows a map from a disk metallized region of a polycrystalline detector (total diamond size 1 × 1 $cm^2$ × 500 µm), pCVD from Element 6. The diamond was biased at -500 V. A piece of the diamond surface (1 $mm^2$) was characterized with a position step size of 8.3 µm and the signal integration time at each point was set to 200 ms. The colour scale corresponds to the charge collection efficiency measured by the Keithley electrometer whose gain was set in auto range. Consequently, the vertical scale is displayed in arbitrary units. In fact, the case presented here corresponds to the worst signal response variations

measured, chosen to show good contrast in the image. Clearly, the response of the detector reflects the spatial distribution of grain boundaries in the polycrystalline material under the micro-focussed X-ray beam. In this sample a factor 6 of difference is observed between the highest signal response (some few hot spots scattered on the whole surface) and the lowest signal response areas. Such results confirmed the previous analysis reported in [45] which was obtained on the same beamline at ESRF in 2002. The sensitivity maps of a 300-µm-thick commercially available pCVD detector grade diamond, metallized with gold contacts and exhibiting an average 80–100 µm grain size range on both sides, were shown in [45], and the authors concluded that current measurement exhibited very strong variations that were associated with the grain boundaries within the material.

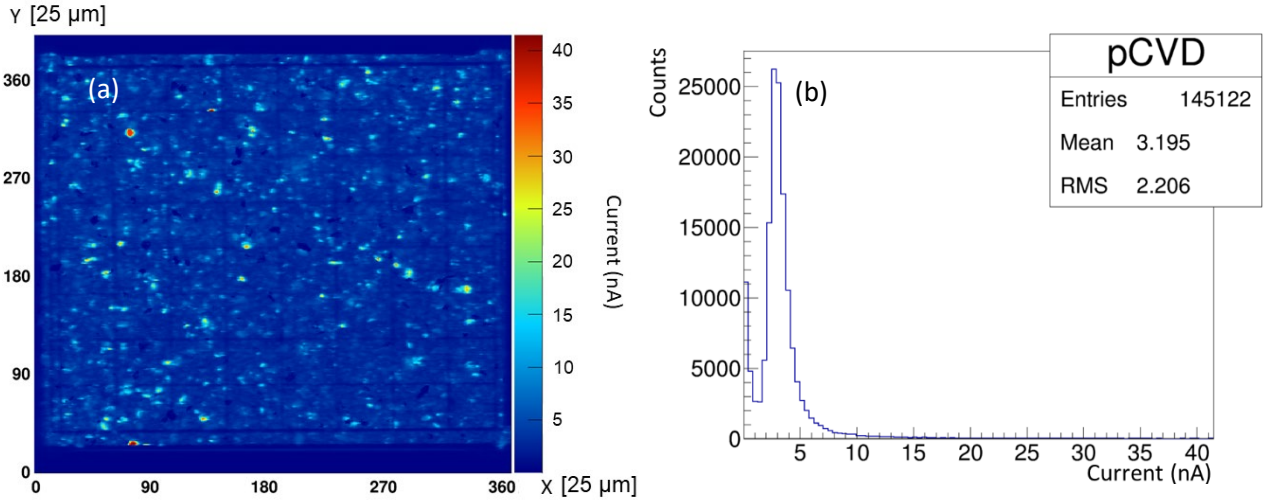


Figure 9 Histogram of the measured current normalized to $\Phi_{32mA}(ph) = 1.79\ 10^9$ ph/s (b) on the surface map (a) [32] of a double side striped $1 \times 1\ cm^2 \times 300\ \mu m$ pCVD diamond detector from Element 6

Figure 9 shows the striped pCVD detector map (1 × 1 cm²× 300 µm detector from Element 6) calibrated according to the method described in section 2.5. The whole diamond surface was characterized with a position step size of 25 µm and the signal integration time at each point was set to 100 ms. The diamond was biased at +300 V. The non-uniformity of the diamond response as indicated by the colour scale on the right reflects some hot spots (as observed in Figure 8) distributed homogeneously over the surface and demonstrates the grain boundary distribution in the diamond material, itself resulting from the pCVD diamond growth [46]. The authors of [47] observed in similar conditions under micro X-ray beam radiation, evidence of localised space charge build-up mechanisms in CVD diamond, and demonstrated that the observed hot-spots could be related to the accumulating of charges at defect sites. The presence of these spots did not, however, greatly affect the homogeneity of the detector response. Indeed, the histogram of the current values measured on the entire surface (including the non-metallised areas between the contact strips) exhibit a single peak at ~3 nA, with 2 nA RMS dispersion. Given the theoretical calculation presented in equation (4), for a 300 µm thick diamond we would expect $R_{diamond}$ = 0.35. Assuming a charge collection efficiency of 100% this results in $I_{mean}$ ~58 nA. The experimental results obtained imply that the spatially averaged charge collection efficiency is only 5.5 %, but Figure 9 exhibits a homogenous distribution of "hot spots" in which the mean current reaches up to 40 nA, corresponding to 70 % charge collection efficiency.

### 3.3 Diamond growth on iridium (DOI).

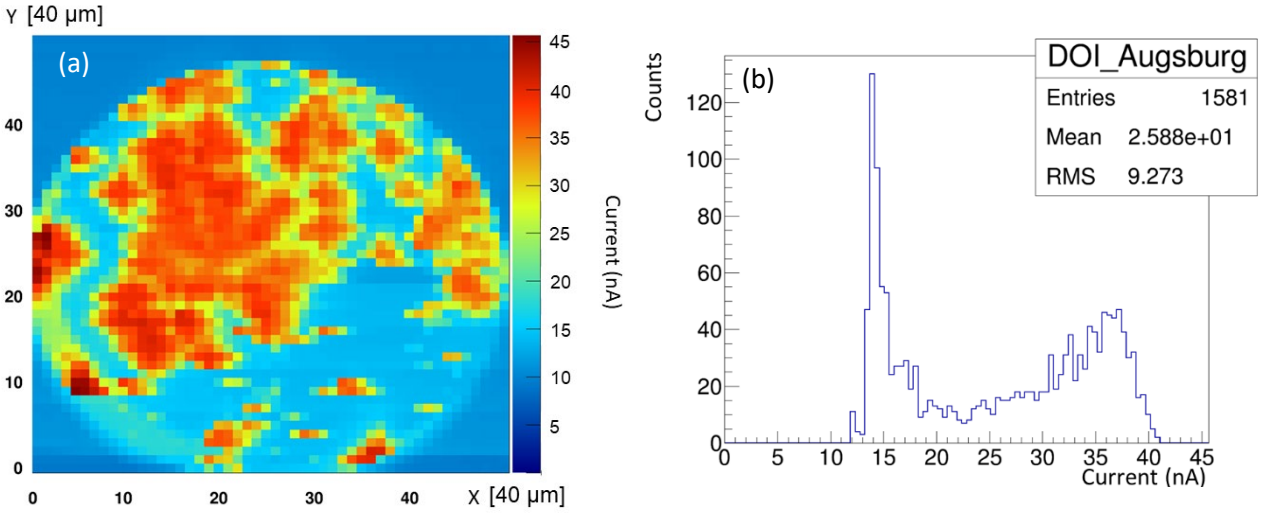


Figure 10 Histogram of the measured current normalized to $\Phi_{32mA}(ph) = 1.79\ 10^9$ ph/s (b) on the surface map (a) of a 0.5× 0.5 cm$^2$ ×300 µm DOI detector from Augsburg University, biased at -300V.

Figure 10 shows a current map done with a disk-metallized 0.5 × 0.5 cm²× 300 µm DOI detector from University of Augsburg, biased at -300 V. The whole diamond surface was characterized with a position step scan of 40 µm, and the data acquisition time on each point was 200 ms. The signal response is clearly inhomogeneous, as illustrated by the colour map and the histogram of the current distribution obtained for the entire disk-metallized diamond surface. The theoretical response value is at the level of 58 nA, estimated for a constant photon flux of $\Phi_{32mA}(ph) = 1.79\ 10^9$ ph/s, a diamond thickness of 300 µm, and a charge collection efficiency of 100%. In Figure 10 (b) two histogram maxima are observed: a narrow one at ~14 nA corresponding to the low response zones (blue regions on the map), and a broader one at ~37 nA with a long tail towards lower current intensities. It should be mentioned that previous analyses [31] have demonstrated that this type of diamond has good time and energy resolution for measurements that are averaged over the whole diamond surface. The mean value of the distribution on Figure 10 (b) corresponds to a charge collection efficiency of 45 %. In areas coloured red in the response map the charge collection reaches up to 71 %. However, the detector exhibits extensive areas with very reduced current intensity and low collection efficiency (8%) that indicate charge carrier trapping at dislocation sites [48]. In the present experiment, the signal is produced by both electron and hole drift within the sample, so it is impossible to distinguish between electron or hole trapping. However, in reference [49], the transport of both carriers is shown to be affected by dislocations.

In Figure 11 and Figure 12 two surface maps of two different striped DOI diamond manufactured by Audiatec (a spin-off company of the University of Augsburg) of bigger size (1 × 1 cm$^2$) are shown, together with their corresponding X-ray beam transmission maps.

In Figure 11 (a) the DOI-1 diamond was biased at +300 V. The whole diamond surface was measured with a position step of 20 µm and data acquisition time on each point of 200 ms. In Figure 11 (b) and (c), the diamond was biased at -300 V and measured with a position step of 50 µm, and data acquisition time on each point of 100 ms.

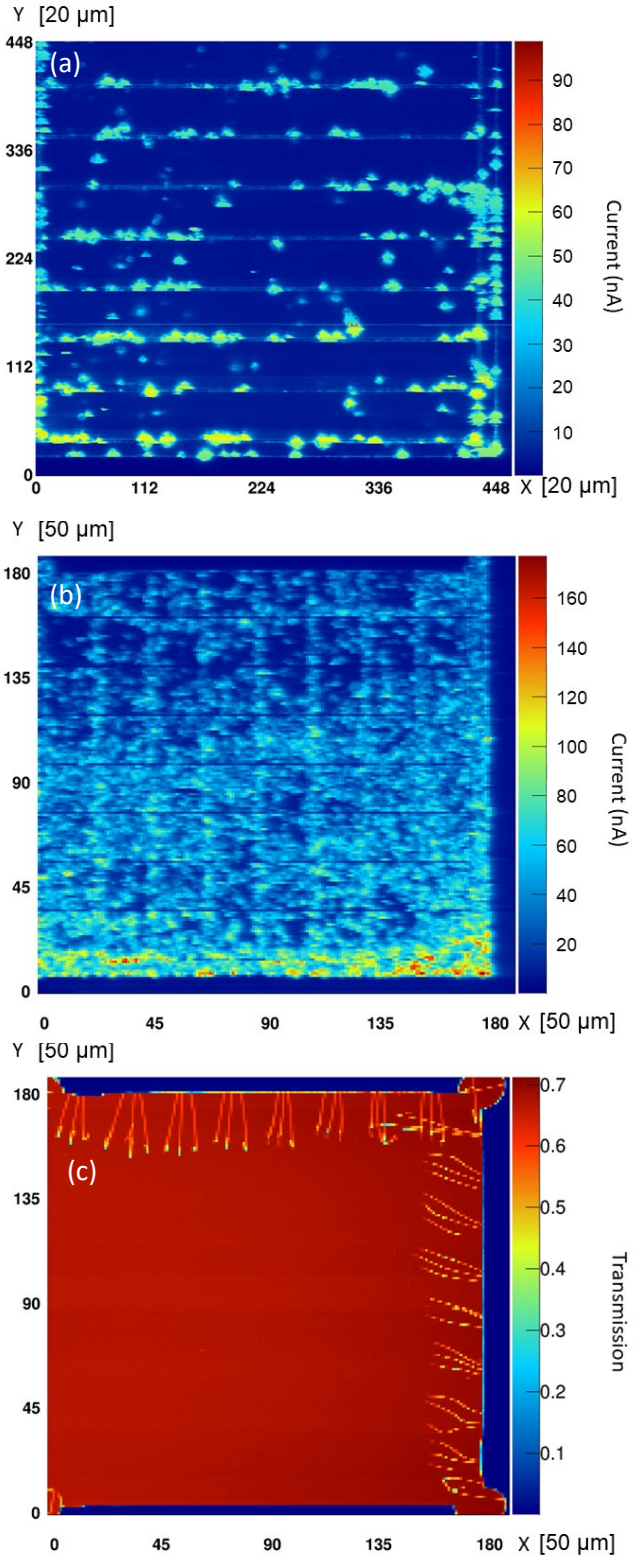


Figure 11 Surface maps of the 1 × 1 $cm^2$ ×300 µm DOI-1 detector from Audiatec, (a) biased at +300 V (b) biased at -300 V, (c) shows the X-ray beam transmission map in which the location of the wire bonds are clearly observed. Results are normalized to $\Phi_{32mA}$(ph) = 1.79 $10^9$ ph/s.

401

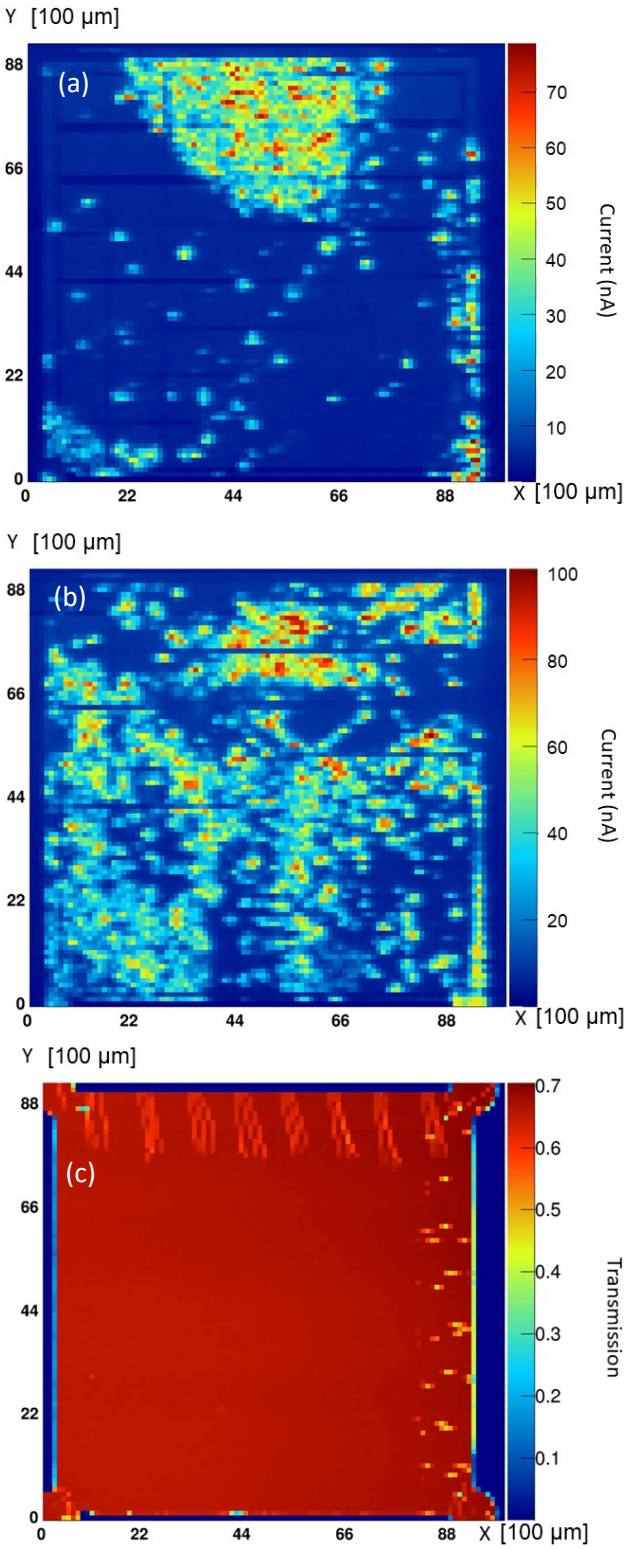


Figure 12 Same as Figure 11, with the 1 × 1 $cm^2$ ×300 µm DOI-2 detector (manufactured by Audiatec) biased at +300 V (a), -300V (b) and the transmission map (c). Results are normalized to $\Phi_{32mA}$(ph) = 1.79 $10^9$ ph/s.

402

In Figure 12 (a), the DOI-2 diamond with non-regular strip spacing (see Figure 5 (b)), was biased at +300 V and in Figure 12 (b) at -300 V. The whole diamond surface was characterized in both cases with a position step of 100 µm and a data acquisition time on each point of 200 ms.

In both Figure 11 (a) and (b) and Figure 12 (a) and (b) we observe that the DOI calibrated maps show inhomogeneous current distribution over the diamond surface, as also shown in Figure 10. For each DOI sample, the (a) and (b) maps were obtained using the same magnitude of diamond bias voltage but applied with opposite sign. The comparison of DOI-1 (a) versus (b) and DOI-2 (a) versus (b), reveals obvious discrepancies in the current distributions. A complete review of the results obtained with DOI diamond samples is given in [50], where the authors demonstrated that in DOI, the transport of the holes is efficient whereas electron transport is poor. This obviously corroborates our present results. Indeed, either the horizontal or vertical electrodes show higher contrast in Figure 11 (a) and (b) and Figure 12 (a) and (b), depending on the chosen bias, as we would expect if a single type of carrier contributes to the observed signal. If the two charge carriers were collected with equal efficiencies, then on the same map we would not be able to distinguish between the two types of electrodes.

The alignment of hot spots along the right vertical edge of the detectors, Figure 11 and Figure 12, corresponds to the presence of wire bonds which caused an enhancement of the XBIC signal, as already observed in [48]. The transmission maps, Figure 11 (c) and Figure 12 (c), obviously show this same contrast due to X-ray absorption in the Al wire bonds, which results in the production at the bond interface of more hot, ionizing electrons. However, the higher signals observed were also likely to result from the 'damage' at the diamond-metal interface resulting from the mechanical impact of the Al wedge wire bonding process. As pointed out above, on Figure 11 (a) and (b), the shape of the electrodes can be clearly distinguished. The darker areas reflect a defect in the collection of charges in the inter-strip region. This can be seen very clearly in the case of DOI-2 (Figure 12 (a) and (b)) where the size of this inter strip spacing varies from 50 µm to 200 µm. Indeed, it was possible to demonstrate by simulation (COMSOL Multiphysics [51]) that the electric field decreases between two adjacent electrodes which results in a significant decrease in the observed current. This is also visible in Figure 9 for the pCVD diamond. This implies that if we want to improve the charge collection, it will be necessary to reduce the inter strip width (see section 4). The significant increase in the signal at each electrode edge reflects a local increase of the electric field. The consequence of reversing the polarity is that the same type of carrier will no longer be collected by a vertical electrode (for example), but instead by a horizontal electrode. In the case of DOI diamonds, if we assume that only the hole charge carriers are collected with high efficiency, then the observation that the horizontal and vertical electrodes do not show equal contrast could reflect the "blocking", Schottky-like nature of the aluminum contacts. We note that the observed differences in diamond signal response for positive or negative high voltage biasing of the sample is not specific to the DOI samples, since it was also obvious in the other samples. Indeed, leakage currents show an asymmetry in Figure 2. Furthermore, after we obtained the present XBIC results, tests using EBIC (Electron Beam Induced Current) carried out at the Institut Néel, Grenoble, on samples of monocrystalline diamonds suggest that the choice of aluminum for the electrodes results in Schottky-like contacts of varying quality which likely explain the asymmetry. A study on improving contacts is underway.

For both DOI-1 and DOI-2 diamonds biased at -300 V, the histograms of the $I_{mean}$ current over the metalized diamond surface are displayed in Figure 13. As before, the theoretical signal value is 58 nA, estimated assuming a constant photon flux of $\Phi_{32mA}(ph) = 1.79\ 10^9$ ph/s, a diamond thickness of 300 µm and a charge collection efficiency of 100%. DOI-1 shows a broad peak (similar to that of Figure 10 (b)) whereas DOI-2 shows a narrower single peak with a long tail spreading to higher current values. In Figure 13 (a), the mean value is 34.16 nA, corresponding to a charge collection efficiency of 60 %, whereas in Figure 13 (b) it reaches only 40 %. Such analyses confirm the results already observed with the smaller disk-metallized diamond, laboratory measurement with alpha particles [37] and results from [50] and seem very representative of the varying area distribution of dislocation densities in diamond grown on iridium, unlike the previous pCVD sample tested in the same conditions.

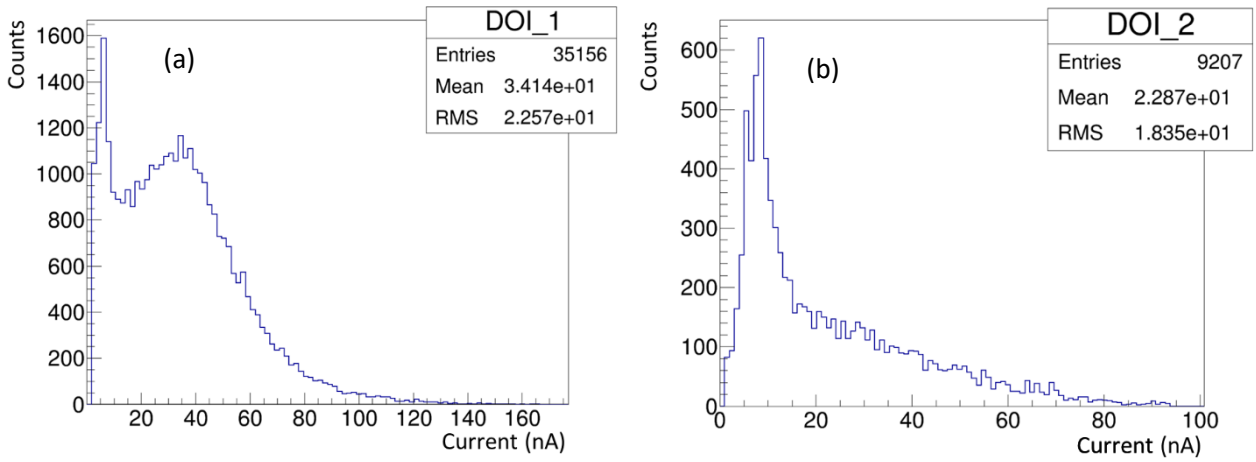


Figure 13 Histogram of the $I_{mean}$ current over the diamond surface on the two different 1 × 1 $cm^2$ × 300 µm DOI samples (DOI-1 (a) and (b) DOI-2) biased at -300 V. Results are normalized to $\Phi_{32mA}$(ph) = 1.79 $10^9$ ph/s.

### 3.4 Compared performances and diamond selection to equip the first prototype of beam hodoscope.

On the one hand, the measured inhomogeneity of the striped DOI-1 and DOI-2 diamond current maps at ESRF with 8.5 keV X-rays pulses was found to be prohibitive to envisage the readout of this diamond type with striped electrodes as foreseen in the planned hodoscope design. Indeed, the signal amplitude will depend on the location where the particle interacts in the DOI. In the best cases we reached 70% of charge collection efficiency. Depending on the type of particle and its energy that we want to detect, this may lead to varying detection efficiency.

On the other hand, the sCVD diamond exhibited excellent performance but the available size for 'off the shelf' detectors are still very small. In order to cover close to 1 $cm^2$ area four 0.45×0.45 $cm^2$ sCVD diamond are necessary to be assembled in a mosaic arrangement.

Such an assembly is to be considered in the future but at first it was decided to choose the 1×1 $cm^2$ pCVD detector to equip the first hodoscope prototype and to evaluate its performances in terms of detection efficiency and time resolution under 8.5 keV X-ray pulsed beams.

## 4. Performances of the pCVD diamond based first hodoscope prototype in pulse mode.

In this part of the work our objective was to select X and Y strips and to scan them with the micro focused beam. We aimed to evaluate, at each micro-beam location, two parameters: the striped pCVD detector X-ray detection efficiency and time resolution. By detection efficiency, we mean the capability of the detector to act as a trigger on a measurable amplitude signal, using a fixed threshold above background level. Our goal was to study the impact of the presence of the observed inhomogeneities on these two parameters which would affect in-beam performance of the future diamond hodoscope we plan to build.

### 4.1 X-ray detection efficiency measured over various top-bottom strips crossing at micro-beam positions.

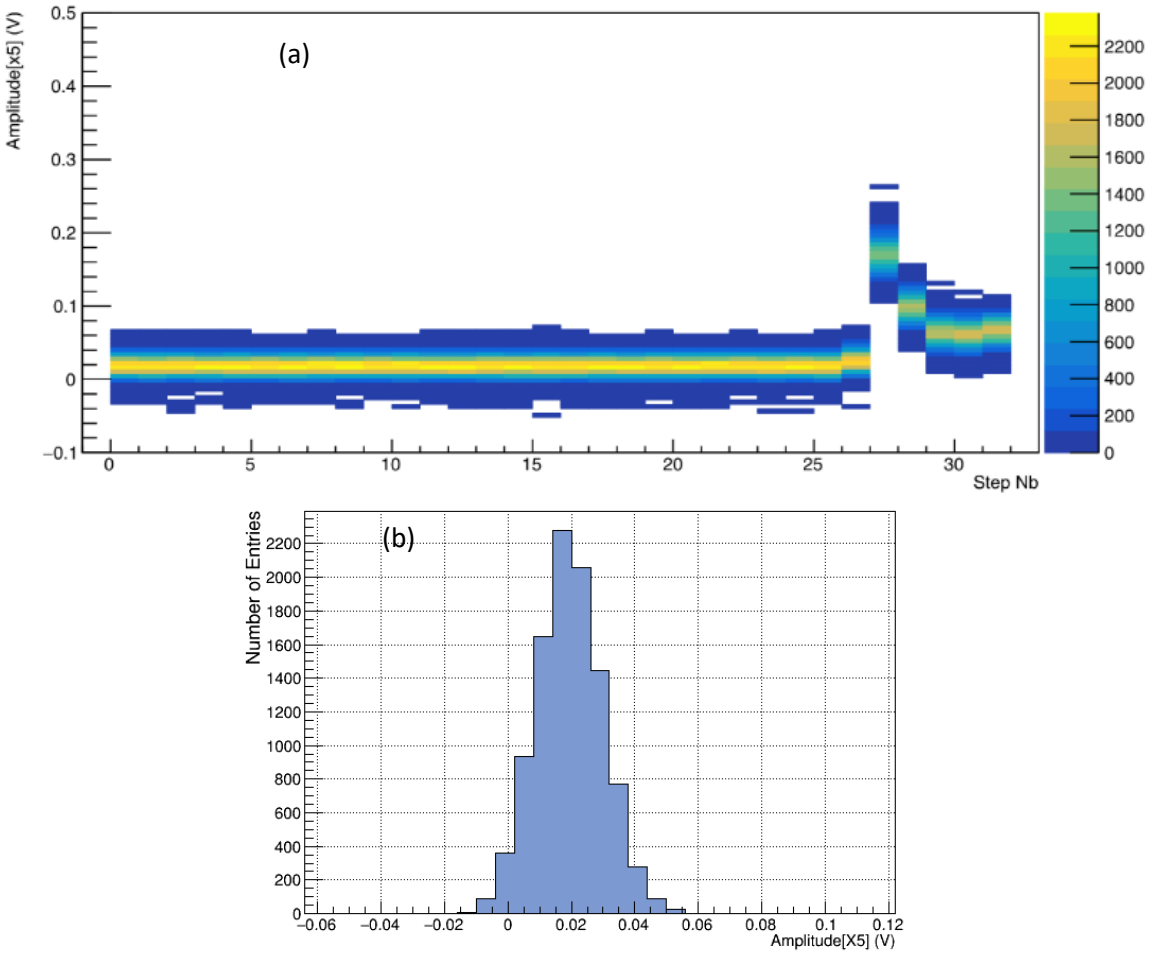


Figure 14 The maximum amplitude on strip X5 displayed for all irradiation positions labelled in step number (a), and the corresponding Y projection at step number 17 (b).

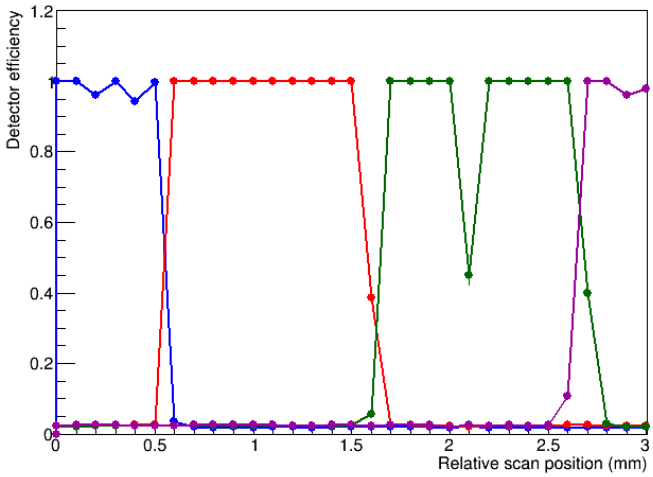


Figure 15 X-ray detection efficiency measured with the striped $1 \times 1\ \mathrm{cm}^2 \times 300\ \mu\mathrm{m}$ pCVD diamond from Element 6 (step size 100 µm, interstrip size 100µm).

To carry out this analysis, 4 strips in X (namely X2, X3, X4, X5) and 1 strip in Y of the prototype hodoscope were connected to the Wavecatcher data acquisition system (see Figure 3 (c)). As previously explained, an external timing trigger was provided by the synchrotron storage ring radio frequency. A horizontal scan on the 4 strips in X was done with 100 µm position steps with signal responses acquired for $10^5$ X-ray pulses at each position step. It should also be noted that, as the scan step is equal to the size of the inter strip, at most we expect to have a single point of measurement at this location. The detector was biased at -500 V (1.6 V/µm) to further improve signal charge collection. Figure 14 (a) shows the amplitude distribution of strip X5, for 32 different irradiation positions (Step Number). When X5 was not irradiated, i.e. from step numbers 0 to 26, the amplitude corresponds to electronic noise. The diamond noise response is rather uniform for the different irradiation positions. In Figure 14 (b), the histogram of amplitudes registered at the step number 17 is shown as an example. The efficiency has been calculated for each strip and for each incident position as the ratio between the number of detected X-ray pulses per number of trigger events. The number of detected X-ray pulses corresponded to the number of signals above a fixed threshold of 40 mV, which, according to Figure 14, was the optimum level to avoid excessive triggering on electronic noise. Results are shown in Figure 15 as a function of the X-axis hit coordinate. The various colours correspond to efficiencies for adjacent strips of the diamond detectors.

As observed in Figure 15, the strip detection efficiency is very close to 100% as evaluated over four adjacent strip crossings, except in the strip gaps: for one gap position (x= 0.6 mm), the efficiency is 1, for the two others it falls to 30-35% (x=1.7 mm, x= 2.8 mm) on only one of the two adjacent strips involved in charge sharing (no cross talk between adjacent strips). This result motivates us to decrease the inter strip gap for the next version of the prototype. The point at position = 2.2 mm with 40 % may correspond to a very localized defect on the strip. We can certainly link this local result to the X-BIC 2D maps made on the same detector. The current integration response map in Figure 9 shows the relative heterogeneity of the response of the detector (and therefore of its charge collection capacities) as a function of the part of volume irradiated. It is possible that this lack of detection efficiency is due to irradiation of an area of lower response on the detector surface. Apart from this singular point, the response of this detector remains relatively homogeneous as far as fixed threshold discrimination is used.

### 4.2 Time resolution measured over various top-bottom strips crossing at different micro-beam positions.

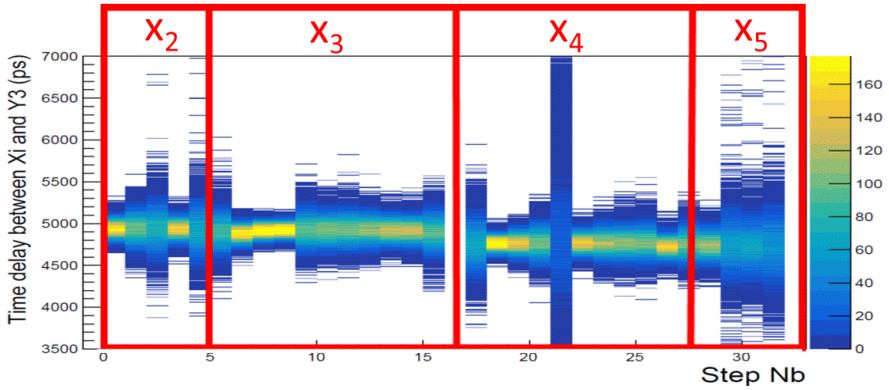


Figure 16 Time distribution over each micro-beam position on Xi-Y3 strip crossing (materialized by the red lines) with i ranging from 2 to 5.

In this experiment, the selected Y strip remains the same (Y3) but the X strips vary over the surface detector as described in the previous section (from X2 up to X5). The waveforms were recorded as before for the X-ray detection efficiency measurement. In total, $10^5$ beam pulses were recorded at each step corresponding to the micro-beam position over the considered strips crossing. To obtain the time resolution, a numerical Constant Fraction Discrimination (CFD) was used by averaging the background on each waveform for the calculation of the baseline, determining the maximum height of the pulses and interpolating the 50 % rise time value (Figure 16). The distribution of the time difference measured simultaneously for the two faces of a detector was characteristic of the time jitter of the readout chain connected to the detector. Figure 17 (b) illustrates this jitter measured on step strip crossing number 14 located on X3 (average of $10^5$ points). This point was chosen as a representative average, with a standard deviation of 108 ps deduced from a Gaussian fit. Figure 17 (a), shows the time resolution 65 ps RMS measured on one of the best cases, step number 8.

The correlation between the average signal amplitude and the time resolution (each point in the graph is the average of $10^5$ recorded X-ray pulses, as for strip crossing number 14 in Figure 17) is shown in Figure 18. The X-axis error bars indicate the RMS of the signal amplitude distribution as measured at

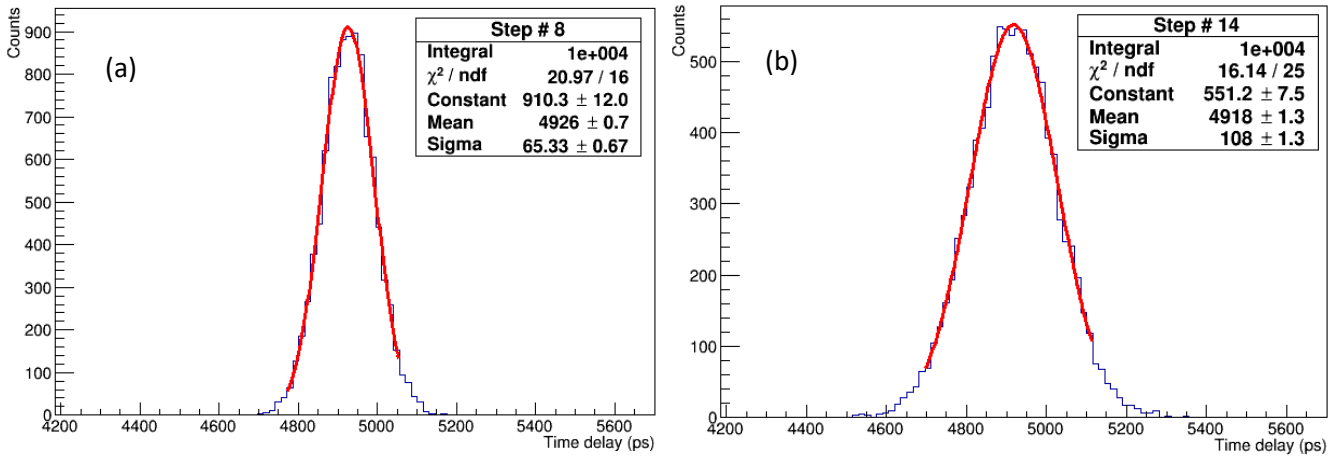


Figure 17 Time resolution (Gaussian fit) measured on step number 8 (strip crossing X3 – Y5) (a) and on step number 14 (b) for changing micro-beam positions on the pCVD detector.

each micro-beam position step number. The error in time resolution is the uncertainty on the fit relative to the standard deviation parameter. In the present experiment, the deposited energy is constant and is linked to the diamond thickness but the charge collection efficiency varies from one point to another on the diamond surface (XBIC experiment) resulting in a variation of the signal amplitude. The adjustment was made by a function proportional to the inverse of the maximum amplitude of the signal. It can be clearly observed that the data are well fitted by such a function. It implies that the collected energy is proportional to the signal amplitude, as expected, and, in addition, that the recorded signal pulses are not degraded at beam positions where the diamond response is lower.

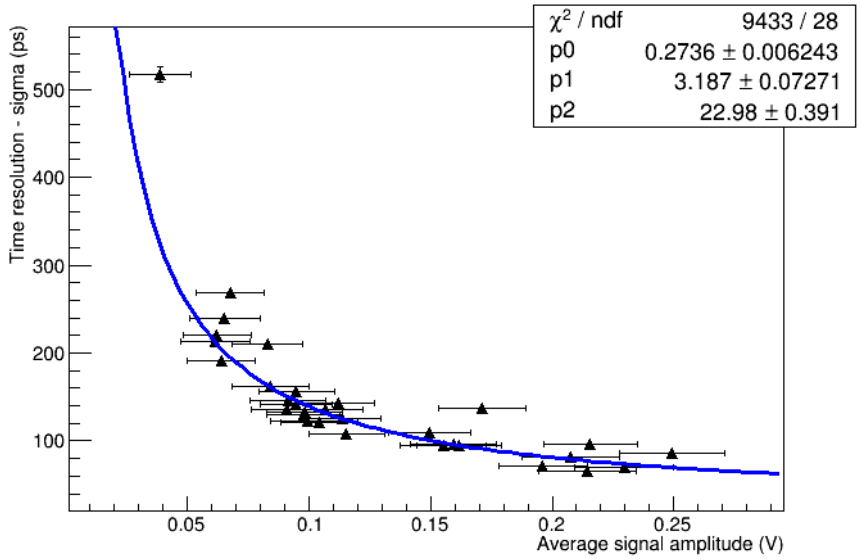


Figure 18 Correlation between the average signal amplitude and the time resolution for beam position over Xi-Y3 with i ranging from 2 to 5 (each point is the average of $10^5$ X-ray pulses). Error bars in the Y direction are within the point size.

Figure 19 shows the observed time resolution (sigma = RMS) as a function of step number (micro beam position). The error shown on the y-axis is the error on the fit for the sigma parameter. The scatter of results correspond to a time resolution ranging from 60 ps to 260 ps if we exclude the singular point already observed in previous plots. Although the distribution among the various tested points is large, the barycentre of the point cloud is 150 $\pm$ 87 ps, a value we are specifically seeking to achieve with the future beam hodoscope. It should be noted that in this readout system, in particular the preamplifiers, has not yet been optimized, and we are confident that a timing resolution below 100 ps can be obtained for carbon ion beams. In the present case, the energy deposit per pulse is 3.4 MeV at maximum (just after the storage ring refill). For proton beams, where the energy deposit per single proton is below 1 MeV, such a setup will be able to detect bunches of several tens of protons with the desired efficiency and time resolution.

In comparison, the time resolution between the two faces of the disk metallized sCVD diamond studied in paragraph 3.1 was found to range between 25.1 ps (CIVIDEC C2) and 53.8 ps (LPSC), i.e. depending on the type of current-voltage preamplifier used (more details are given in reference [32]). There is about a factor 2 of difference that relies on the readout electronic fast preamplifier. Furthermore, the 1 × 1 cm² × 500 µm pCVD results shown in Figure 8, with disk-metallization and higher detector thickness (500 µm instead of 300 µm) exhibited a time resolution of ~72 ps using readout by two CIVIDEC C2 preamplifiers, as reported in reference [32]. So we can conclude that all these results are consistent and that a means to further improve this resolution will be to improve our fast front-end readout electronics.

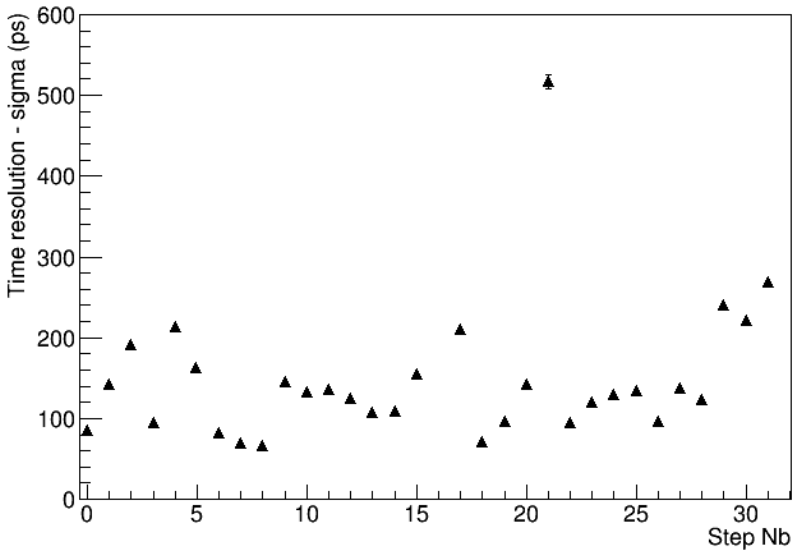


Figure 19 Time resolution versus Step number which corresponds to the beam position over Xi-Y3 with i ranging from 2 to 5 (each point is the average of $10^5$ points). Error bars are within the point size.

## 5. Summary and discussion on measured performances in XBIC in the perspective of the future beam tagging hodoscope development for hadrontherapy monitoring.

In the first part of the XBIC measurements, the three types of diamond samples sCVD, pCVD and DOI were tested in current mode. This enabled an evaluation of their performance in terms of charge collection efficiency over their entire surfaces, as probed by a micron size beam probe measuring every few tens of microns. Laboratory experiments on an alpha particle test bench had already made it possible to demonstrate that the charge collection efficiency of the sCVD diamond was 100% while that of pCVD gave an area average of 30% and that of DOI 40% [37]. However, these experiments were made with a radioactive source, so that the impact of the alpha particles on the surface of the diamond are at low rates and random in time and spatial position. In consequence these measurements do not sufficiently account for possible detector inhomogeneities. Therefore the measurements at the ESRF provided us with additional knowledge on performance of diamonds as regards their spatial (non-) homogeneity. This "homogeneity" parameter is a fundamental criterion for the hodoscope design involving a position sensitive detector and whose development in terms of position calibration must not present any major difficulty. In addition, the tunable intensity 8.5 keV X-ray pulses represented a maximum energy deposit of 3.4 MeV and 5.2 MeV for diamond thicknesses of 300 and 500 µm, respectively. This corresponds to a collected charge of 40 and 61 fC (if we assume a collection efficiency of 100%), a similar energy deposition that of a 400MeV/nucleon carbon ion beam in a 500 µm thick diamond detector with an average charge collection efficiency of 30%. Such a beam is very likely to be used in hadrontherapy. The measurements carried out at the ID21 beamline are therefore completely transposable to one of the future applications targeted by the hodoscope, and are a good indicator of its performance.

In a second part of the XBIC measurement, we made pulse measurements on the micrometer scale with the pCVD demonstrator we selected thanks to the current map analysis. These measurements allowed

us to probe the detection efficiencies and to have time resolution estimates as a function of the point of impact of the ionizing beam on the strip crossings. Previous measurements carried out under conditions similar to those at the ESRF with disc metallized detectors coupled to three types of fast current - voltage preamplifiers (two from different manufacturers often cited in the literature for reading diamond signals, and one previously developed at LPSC used to readout the demonstrator discussed in this work) have enabled us to make comparisons [32]. If we look in detail at the time resolution distribution on the strip crossing, we can confirm that in certain points identified in the first part of the tests as "hot spots", the time resolution of the polycrystalline diamond approaches that measured with the single crystal diamonds in a previous experiment. We also conclude that for these measurements the performance of the electronic readout system is crucial and is an area requiring further work by us. Finally, at the strip crossings, the average time resolution is $150 \pm 87$ ps RMS for an energy deposit of 3 MeV. As a consequence, we are confident of obtaining a timing resolution below 100 ps for carbon ion beams with a slightly improved version of the present electronics. With protons of 70 MeV, which is an energy used in certain clinical centers to treat eye tumors, the estimated energy deposit is 1 MeV, so it will be possible to detect bunches of several tens of protons with the desired efficiency and time resolution resolution (then the time resolution will be dominated by the bunch duration, not by the diamond).

All of these results motivate us to consider new developments in electronics. Since these experiments have been carried out, a new preamplifier design has been achieved in 2020 with improved performance. The gain is higher, the noise is comparable and the power consumption has been reduced more than 10-fold. This power reduction makes feasible the mounting of several chips in close proximity to the diamond strips leading to a higher-performance readout.
Furthermore, we are currently considering a solution consisting of an assembly of 4 monocrystalline diamonds of surface $0.45 \times 0.45$ mm$^2$ (4 sCVD beam monitor) in order to better improve charge collection efficiency and thus to be able to meet the above specifications for the detection of single protons. The new experimental set-up under construction is intended for testing with 70 MeV protons at the ARRONAX facility in Nantes-France by the end of the year 2020. In addition, we have recently published first results on Prompt Gamma Timing with about 100 ps RMS Time of Flight resolution, using a fast monolithic scintillators and a single crystal diamond-detector beam trigger [52]. This result was obtained in ARRONAX with 70 MeV proton beam. Consequently, such a result makes us confident about the performance of the new 4 sCVD beam monitor version which we are currently developing.

## 6. Conclusion

Several diamond samples were tested under XBIC micro-beams. 2D maps have been drawn. Single crystal sCVD diamonds have shown a very homogeneous response. The pCVD diamonds show a scattered location of hot spots. However, the overall response of the detector is also very homogeneous. On the contrary, diamonds on iridium show very great inhomogeneity on the surface with large areas of defects.

The striped pCVD diamond was chosen to equip the first diamond based beam hodoscope. It was tested under X-rays. Results obtained are encouraging for the aimed development of a beam-tagging hodoscope with ToF capabilities. The various strip crossing tested showed time resolutions at the level of the targeted value of 100 ps RMS with excellent particle detection efficiency.

However, preserving an excellent ToF resolution at high proton energies seems challenging, particularly for pCVD. Another solution may consist in using either large area sCVD diamonds or a mosaic arrangement of sCVD. Large area sCVD are not commercially available at the moment but CVD diamond growth technologies progress quickly [53]. The next step of the development is then the assembling of four selected diamonds with optimized electronics for further characterization and tests under irradiation conditions close to clinical ones.

**Acknowledgments**

The authors would like to acknowledge the ESRF-ID21 beamline for provision of synchrotron radiation with experiments MI-1243 (2016) and MI-1285 (2017), and support from the ESRF BLISS group for integrating the triggered readout of the Lecroy DSO into the ID21 SPEC data acquisition system This work was supported by the Labex PRIMES (ANR-11-LABX-0063), FranceHadron (ANR-11-INBS-0007) and the ANR MONODIAM-HE (ANR-089520) and ITMO-Cancer (CLaRyS-UFT project). It was performed in the frame of ENSAR2/MediNet network (Horizon2020-654002). The authors are grateful to Matthias Schreck from Augsburg University and Martin Fischer from Audiatec-Augsburg for providing the LPSC laboratory with DOI samples. Dominique Breton and Jihanne Maalmi from LAL-Orsay and Eric Delagnes from CEA Saclay are thanked for their implication in dedicated software development and technical support of the Wavecatcher data acquisition system.

**References**

[1] H. Pernegger, S. Roe and P.Weilhammer, "Charge-carrier properties in synthetic single-crystal diamond measured with the transient-current technique", Journal of Applied Physics, Volume 97, Issue 7, p 073704, 2005. https://doi.org/10.1063/1.1863417.

[2] M. Pomorski, E. Berdermann, A. Caragheorgheopol, M. Ciobanu, M. Kiš, A. Martemiyanov, C. Nebel and P. Morit, "Development of single-crystal CVD-diamond detectors for spectroscopy and timing", Physica Status Solidi (A), Applied Research, Vol 203, Issue 12, pp 3152-3160, 2006. https://doi.org/10.1002/pssa.200671127

[3] E. Griesmayer and B. Dehning, "Diamonds for beam instrumentation", in Proceedings of the 2nd International Conference on Technology and Instrumentation in Particle Physics (TIPP 2011), Chicago U.S.A. (2011) [Physics Procedia, Volume 37, 2012, pp 1997 - 2004] https://doi.org/10.1016/j.phpro.2012.02.526

[4] C. Verona, G. Magrin, P. Solevi, M. Bandorf, M. Marinelli, M. Stock, and G. V. Rinati. Toward the use of single crystal diamond based detector for ion-beam therapy microdosimetry. Radiation Measurements, Volume 110, March 2018, Pages 25–31. https://doi.org/10.1016/j.radmeas.2018.02.001

[5] https://www.ptwdosimetry.com/en/products/microdiamond/

[6] J. Livingstone, A W. Stevenson, D. J. Butler, D. Häusermann and J.-F. Adam, "Characterization of a synthetic single crystal diamond detector for dosimetry in spatially fractionated synchrotron x-ray fields", Medical Physics, 2016, 43(7): 4283. https://doi.org/10.1118/1.4953833

[7] I. A. Zahradnik, M. Pomorski, L. De Marzi, D. Tromson, P. Barberet, N. Skukan, P. Bergonzo, G. Devès, J. Herault, W. Kada, T. Pourcher, and Samuel Saada, "scCVD Diamond Membrane based Microdosimeter for Hadron Therapy", Physica Status Solidi (A), Vol. 215, Issue 22, Special Issue: Diamond Science and Technologie, November 21, 2018 1800383 https://doi.org/10.1002/pssa.201800383

[8] J. Van de Walle, S. Henrotin, Y. Paradis and I.C. tKint," A diamond detector test bench to assess the S2C2 beam characteristics", proceedings of Cyclotrons2016, Zurich, Switzerland, 2016 https://accelconf.web.cern.ch/Cyclotrons2016/papers/mop19.pdf

[9] H. Pernegger, H. Frais-Kölbl, E. Griesmayer, and H. Kagan . "Design and test of a high-speed single-particle beam monitor." Nuclear Instruments and Methods in Physics Research, Section A: Accelerators, Spectrometers, Detectors and Associated Equipment, Volume 535, Issue 1-2, 11 December 2004, Pages 108–114 https://doi.org/10.1016/j.nima.2004.07.213

[10] H. Pernegger "High mobility diamonds and particle detectors." Physica Status Solidi (A) Applications and Materials Science, Volume 203, Issue 13, Special Issue: Selected Topics in Physics and Applications of CVD Diamond, October 2006, pp 3299–3314 https://doi.org/10.1002/pssa.200671404

[11] H. Frais-Kölbl, E. Griesmayer, H. Kagan, and H. Pernegger, "A fast low-noise charged-particle CVD diamond detector" IEEE Transactions on Nuclear Science, Volume 51, Issue 6, December 2004, Pages 3833–3837 https://doi.org/10.1109/TNS.2004.839366

[12] H. Frais-Kölbl, E. Griesmayer., T. Schreiner, D. Georg, and H. Pernegger, "Medical beam monitor—pre-clinical evaluation and future applications" Nuclear Instruments and Methods in Physics Research Section A: Accelerators, Spectrometers, Detectors and Associated Equipment, Volume 581, Issue 1-2, 21 October 2007, Pages 103 – 106. https://doi.org/10.1016/j.nima.2007.07.038

[13] M. Rydygier, M. Jastrzab, D. Krzempek, T. Nowak, I. Grzanka, P. Bednarczyk and L. Stolarczyk, "Radiotherapy proton beam profilometry with scCVD diamond detector in single particle mode." Radiation Protection Dosimetry, Volume 180, Issue 1-4, August 2018, Pages 282-285. https://doi.org/10.1093/rpd/ncx305

[14] J. Krimmer, J.-L. Ley, C. Abellan, J.-P. Cachemiche, L.Caponetto, X.Chen, M. Dahoumane, D. Dauvergne, N. Freud, B. Joly, D. Lambert, L. Lestand, J.M. Létang, M.Magne, H. Mathez, V. Maxim, G. Montarou, C. Morel, M. Pinto, C. Ray, V. Reithinger, E. Testa, Y. Zoccarato, "Development of a Compton camera for medical applications based on silicon strip and scintillation detectors", Nuclear Instruments and Methods in Physics Research A: Accelerators, Spectrometers, Detectors and Associated Equipment, Volume 787, 1 July 2015, Pages 98-101. https://dx.doi.org/10.1016/j.nima.2014.11.042

[15] H. Paganetti, "Range uncertainties in proton therapy and the role of Monte Carlo simulations" Physics in Medicine and Biology, Volume 57, Number 11, pp. R99–R117, Jun 2012. https://doi.org/10.1088/0031-9155/57/11/R99

[16] C.-H. Min, C. H. Kim, M.-Y. Youn, and J.-W. Kim, "Prompt gamma measurements for locating the dose falloff region in the proton therapy," Applied Phyics. Letters, Vol. 89, Issue 18, pp. 183517–3, October 2006. https://doi.org/10.1063/1.2378561

[17] E. Testa, M. Bajard, M. Chevallier, D. Dauvergne, F. Le Foulher, N. Freud, J.-M. Létang, J.-C. Poizat, C. Ray, and M. Testa, "Monitoring the Bragg peak location of 73 MeV/u carbon ions by means of prompt γ-ray measurements," Applied Physics Letter, Volume 93, Issue 9, pp. 93506, 2008. https://doi.org/10.1063/1.2975841

[18] J. Krimmer, D. Dauvergne, J.M. Létang and É. Testa, "Prompt-gamma monitoring in hadrontherapy: a review", Nuclear Instruments and Methods in Physics Research: Accelerators, Spectrometers, Detectors and Associated Equipment, Volume 878, 11 January 2018, pages 58-73. http://dx.doi.org/10.1016/j.nima.2017.07.063

[19] J. Krimmer, M. Chevallier, J. Constanzo, D. Dauvergne, M. De Rydt, G. Dedes, N. Freud, P. Henriquet, C. La Tessa, J.M. Létang, R. Pleskač, M. Pinto, C. Ray, V. Reithinger, M.H. Richard, I. Rinaldi, F. Roellinghoff, C. Schuy, E. Testa and M. Testa, "Collimated prompt gamma ToF measurements with multi-slit multi-detector configurations," Journal of Instrumentation, Volume 10, no. 1, pp. P01011–P01011, January 2015. https://iopscience.iop.org/article/10.1088/1748-0221/10/01/P01011

[20] C. Bauer, I. Baumann, C. Colledani, J. Conway, P. Delpierre, F. Djama, W. Dulinski, A. Fallou, K. Gan, R. Gilmore, E. Grigoriev, G. Hallewell, S. Han, T. Hessing, K. Honschied, J. Hrubec, D. Husson, H. Kagan, D. Kania, R. Kass, W. Kinnison, K.T. Knöpfle, M. Krammer, T.J. Llewellyn, P.F. Manfredi, L.S. Pan, H. Pernegger, M. Pernicka, R. Plano, V. Re, S. Roe, A. Rudge, M. Schaeffer, S. Schnetzer, S. Somalwar, V. Speziali R. Stone, R.J. Tapper, R.Tesarek, W. Trischuk, R. Turchetta, G.B. Thomson, R. Wagner, P. Weilhammer, C. White, H. Ziock, and M. Zoeller. "Radiation hardness studies of CVD diamond detectors." Nuclear Instruments and Methods in Physics Research Section A: Accelerators, Spectrometers, Detectors and Associated Equipment, Volume 367, Issue 1-3, 11 December 2015, Pages 207–211. https://doi.org/10.1016/0168-9002(95)00545-5

[21] A. Crnjac, N. Skukan, G. Provatas, M. Rodriguez-Ramos, M. Pomorski, and M. Jaksic. "Electronic properties of a synthetic single-crystal diamond exposed to high temperature and high radiation. Materials", Materials 2020, 13(11), 2473. https://doi.org/10.3390/ma13112473

[22] N. Tranchant, "Growth and characterization of single-crystal CVD diamond for radiation detection applications", Doctoral thesis, Institut National des Sciences Appliquées (INSA), Rennes France, 2008.

[23] Venturi et al, RD42 collaboration, "Results on radiation tolerance of diamond detectors", Nuclear Instruments and Methods in Physics Research A: Accelerators, Spectrometers, Detectors and Associated Equipment, Volume 924, 21 April 2019, Pages 241-244 https://doi.org/10.1016/j.nima.2018.08.038)

[24] A. Ghimouz, F. Rarbi, L. Gallin-Martel, and O. Rossetto, "A preamplifier-discriminator circuit based on a common gate feedforward TIA for fast time measurements using diamond detectors," 25th IEEE International Conference on Electronics, Circuits and Systems (ICECS), 281–284, Bordeaux, 2018. https://ieeexplore.ieee.org/document/8617950

[25] C. Caplan, O. Allegrini, J. P. Cachemiche, B. Carlus, X. Chen, D. Dauvergne, R. Della Negra, M. Fontana, L. Gallin-Martel, J. Hérault, D. Lambert, G.-N. Lu, M. Magne, H. Mathez, G. Montarou, C. Morel, M. Rodo-Bordera, E. Testa and Y. Zoccarato, 2019. "A µTCA back-end firmware for data acquisition and slow control of the CLaRyS Compton camera", proceedings IEEE MIC conference, Manchester, United Kingdom, 2019. https://doi.org/10.1109/NSS/MIC42101.2019.9059941

[26] https://physics.nist.gov/cgi-bin/Xcom/

[27] R. S. Balmer, J. R. Brandon, S. L. Clewes, H. K. Dhillon, J. M. Dodson, I. Friel, P. N. Inglis, T. D. Madgwick, M. L. Markham, T. P. Mollart, N. Perkins, G. A. Scarsbrook, D. J. Twitchen, A. J Whitehead, J. J. Wilman and S. M. Woollard,"Chemical vapour deposition synthetic diamond: materials, technology and applications", Journal of Physics: Condensed Matter, Volume 21, Number 36 2009 https://doi.org/10.1088/0953-8984/21/36/364221

[28] http://e6cvd.com/

[29] http://www.audiatec.de/

[30] M. Schreck, J. Asmussen, S. Shikata, J.-C. Arnault, and N. Fujimori, "Large-area high-quality single crystal diamond", MRS Bulletin, Vol.39, Issue 6, June 2014, pp. 504-510. https://doi.org/10.1557/mrs.2014.96

[31] M.-L. Gallin-Martel, A. Bes, A. Boukhémiri, G. Bosson, J. Collot, D. Dauvergne, M. Fontana, L. Gallin-Martel, A. Gorecki, JY. Hostachy, J. Krimmer, A. Lacoste, S. Marcatili, J. Morse, JF. Muraz, FE. Rarbi, O. Rossetto, M. Salomé, E. Testa and M. Yamouni, "Large area polycrystalline diamond detectors for online hadron therapy beam tagging applications", proceedings IEEE NSS/MIC conference, Strasbourg, France, 2016 https://doi.org/10.1109/NSSMIC.2016.8069398

[32] M.-L. Gallin-Martel, L. Abbassi, A. Bes, G. Bosson, J. Collot, T. Crozes, S. Curtoni, D. Dauvergne, W. De Nolf, M. Fontana, L. Gallin-Martel, J.-Y. Hostachy, J. Krimmer, A. Lacoste, S. Marcatili, J.

Morse, J.-F. Motte, J.-F. Muraz, F. E. Rarbi, O. Rossetto, M. Salomé, É. Testa, R. Vuiart and M. Yamouni, “A large area diamond-based beam tagging hodoscope for ion therapy monitoring”, invited talk, ANIMMA 2017, Liège, Belgium, published in IEEE, https://doi.org/10.1051/epjconf/201817009005

[33] M. Pomorski, B. Caylar and Ph. Bergonzo,“Super-thin single crystal diamond membrane radiation detectors”, Applied Physics Letter, Volume 103, Issue 11, 112106, 2013. https://doi.org/10.1063/1.4821035

[34] K. Desjardin, D. Duran, S. Hustache, M. Pomorski and W. Shepard, “Charactersation of CVD diamond devices as XBPMs at SOLEIL” 11th International Conference on Synchrotron Radiation Instrumentation (SRI 2012), Journal of Physics Conference Series, Volume 425 (21) https://doi.org/10.1088/1742-6596/425/21/212004

[35] K. Driche,”Diamond unipolar devices : towards impact ionization coefficients extraction”, Doctoral thesis, Université Grenoble Alpes France, 2018

[36] J. Morse, M. Salomé, E. Berdermann, M. Pomorski, W. Cunningham and J. Grant, “Single crystal CVD diamond as an X-ray beam monitor”, Diamond and Related Material, Volume 16, Issue 4-7, April-July 2007, Pages 1049-1052 https://doi.org/10.1016/j.diamond.2006.11.081

[37] S. Curtoni,” Development of a diamond beam-tagging hodoscope demonstrator for online ion range verification in hadrontherapy”, Doctoral thesis, Université Grenoble Alpes France, 2020

[38] A. Lacoste, T Lagarde, S Béchu, Y Arnal and J Pelletier, “Multi-dipolar plasmas for uniform process physics, design and performance”, Plasma Sources Science and technology, Volume 11, Number 4, pp 407-412, 2002 https://iopscience.iop.org/article/10.1088/0963-0252/11/4/307/meta

[39] https://cividec.at/_C2_Broadband_Amplifier,_2_GHz,_40_dB.html

[40] D. Breton, E. Delagne and J. Maalmi, “Picosecond time measurement using ultra-fast analog memories”, proceedings TWEPP2009, Topical Workshop on Electronics for Particle Physics. Paris 21-25 September 2009 https://doi.org/10.5170/CERN-2009-006.149

[41] http://teledynelecroy.com/oscilloscope/

[42] P. Bergonzo, D. Tromson, C. Descamps, H. Hamrita, C. Mer, N. Tranchant and M. Nesladek, ”Improving diamond detectors: A device case” Diamond & Related Materials, Volume 16, Issue 4-7, April – July 2007, Pages 1038–1043 https://doi.org/10.1016/j.diamond.2006.11.099

[43] L. S. Pan, S. Han, and D. R. Kania,Diamond: Electronic Properties and Applications (Kluwer Academic, Dordrecht, 1995)

[44] M. Gaowei, E. Muller, J. Smedley, A.Sumant, T.Zhou, ‘Responsivity Study of Diamond X-ray Monitors with nUNCD Contact’, Jun, 2015, Proceedings, 6th International Particle Accelerator Conference (IPAC 2015), Richmond, VA, USA https://doi.org/10.18429/JACoW-IPAC2015-MOPWI052

[45] P. Bergonzo, R. Barrett, O. Hainaut, D. Tromson, C. Mer, B. Guizard, “Imaging of the sensitivity in detector grade polycrystalline diamonds using micro-focused X-ray beams”, Diamond and Related Materials, Volume 11, March-June 2002, Pages 418-422 https://doi.org/10.1016/S0925-9635(01)00662-8

[46] T. Liu, D. Raabe, W. Mao and S. Zaefferer,”Microtexture and Grain Boundaries in freestanding CVD diamond films: growth and twinning mechanisms”, 2009, Advanced Functional Materials, Volume 19, Issue 24, Pages 3880-3891. https://doi.org/10.1002/adfm.200901231

[47] M.J. Guerrero, D. Tromson, P. Bergonzo and R. Barrett, “Investigation of defects in CVD diamond: Influence for radiotherapy applications”, Nuclear Instruments and Methods in Physics Research A: Accelerators, Spectrometers, Detectors and Associated Equipment, Volume 552, Issue 1-2, October 2005, Pages 105–111 https://doi.org/10.1016/j.nima.2005.06.015

[48] M. Pomorski, “Electronic Properties of Single Crystal CVD Diamond and its Suitability for Particle Detection in Hadron Physics Experiments”, Doctoral Thesis, Frankfurt University, 2008

[49] A. Lohstroh, P. J. Sellin, S. G. Wang, A. W. Davies, and J. M. Parkin, “Mapping of polarization and detrapping effects in synthetic single crystal chemical vapor deposited diamond by ion beam induced charge imaging”, Journal of Applied Physics, Volume 101, Issue 6, p 063711, 2007. https://aip.scitation.org/doi/10.1063/1.2653669

[50] E. Berdermann, K. Afanaciev, M. Ciobanu, M. Fischer, S. Gsell, M. Kiš, S. Lagomarsino, W. Lohmann, M. Mayr, M. Pomorski, M.S. Rahman, C.J. Schmidt, S. Sciortino, M. Schreck, C. Steh, M. Träger, The NoRHDia, CARAT, and ADAMAS Collaborations “Progress in detector properties of heteroepitaxial diamond grown by chemical vapor deposition on Ir/YSZ/Si(001) wafers.”, Diamond and Related Materials, Volume 97, August 2019, 107420 https://doi.org/10.1016/j.diamond.2019.05.006

[51] COMSOL Multiphysics® https://www.comsol.fr/

[52] S. Marcatili, J. Collot, S. Curtoni, D. Dauvergne, J.-Y. Hostachy, C. Koumeir, J.-M. Létang, J. Livingstone, V. Metivier, L. Gallin-Martel, M.-L. Gallin-Martel, J.-F. Muraz, N. Servagent, E. Testa and M. Yamouni “Ultra-fast prompt gamma detection in single proton counting regime for range monitoring in particle therapy.”, accepted for publication in Physics in Medicine and Biology (2020) https://doi.org/10.1088/1361-6560/ab7a6c

[53] J. Achard, LSPM Villetaneuse France, private communication.